Contrib Mineral Petrol (2004) 147: 647–670
DOI 10.1007/s00410-004-0582-2

ORIGINAL PAPER

Giorgio Rivalenti · Alberto Zanetti
Maurizio Mazzucchelli · Riccardo Vannucci
Carlos A. Cingolani

Equivocal carbonatite markers in the mantle xenoliths of the Patagonia backarc: the Gobernador Gregores case (Santa Cruz Province, Argentina)

Received: 2 February 2004 / Accepted: 14 April 2004 / Published online: 13 July 2004

Abstract Amphibole ± phlogopite ± apatite-bearing mantle xenoliths at Gobernador Gregores display modal, bulk-rock and phase geochemical characteristics held as indicators of carbonatitic metasomatism. However, part of these xenoliths has high TiO_2/Al_2O_3 and those displaying the most pronounced carbonatitic geochemical markers modally trend towards harzburgite. Bulk-rock, clinopyroxene and amphibole show Zr, Hf and Ti negative anomalies, which increase at decreasing Na_2O and high field strength elements (HFSE) concentrations. Steady variation trends between xenoliths which have and do not have carbonatitic characteristics suggest a control by reactive porous flow of only one agent, inferred to be initially a ne-normative hydrous basalt (because of the presence of wehrlites) evolving towards silica saturation. Variation trends exhibit cusps when amphibole appears in the mode. Appearance of amphibole may explain the Ti anomaly variations, but not those of Zr and Hf. Numerical modelling [Plate Model (Vernières et al. in J Geophys Res 102:24771–24784, 1997)] gives results consistent with the observed geochemical features by assuming the presence of loveringite. Modest HFSE anomalies in the infiltrating melt may be acquired during percolation in the garnet-facies.

In memory of Carlo Rivalenti

G. Rivalenti (✉) · M. Mazzucchelli
Dipartimento di Scienze della Terra,
Università di Modena e Reggio Emilia,
P.le S. Eufemia, 19, 41100 Modena, Italy
E-mail: riva@unimore.it
Tel.: +39-59-2055813
Fax: +39-59-2055898

A. Zanetti · R. Vannucci
Dipartimento di Scienze della Terra,
Università di Pavia and CNR,
Instituto di Geoscienze e Georisorse,
Sezione di Pavia, Via Ferrata, 1,
27100 Pavia, Italy

C. A. Cingolani
Centro de Investigaciones Geológicas,
Universidad Nacional de La Plata, 644 Calle No. 1,
1900 La Plata, Argentina

Introduction

This paper discusses how far modal and geochemical characteristics of mantle xenoliths are reliable indicators of a given metasomatic agent, in the study case carbonatite. Since the studies of Green and Wallace (1988), Wallace and Green (1988), Yaxley et al. (1991) and Dautria et al. (1992), safe mineralogical and geochemical markers of carbonatite metasomatism in spinel-facies mantle xenoliths are considered to be: (1) modal variation trend towards wehrlite (Dalton and Wood 1993); (2) presence of apatite; (3) high Na, Cr, Mg# and light rare Earth elements (LREE) in clinopyroxene; (4) large light REE/heavy REE (LREE/HREE) fractionation, marked Zr, Hf and Ti depletion with respect to REE (e.g. Chazot et al. 1994), and, although less commonly used, low Th/U in clinopyroxene (Foley et al. 2001), high Nb/Ta and Zr/Hf (Rudnick et al. 1993; Green 1995) in the bulk-rock. These modal and geochemical features are frequent in xenolith occurrences of any geotectonic environment. Thus, carbonatite has become a very popular, ambient-independent, metasomatic agent modifying the mantle lithosphere.

Comparison with natural carbonatites and experimental work on the partition coefficients between silicic and carbonatitic melts and silicate phases (Wendlandt and Harrison 1979; Sweeney et al. 1992, 1995; Green et al. 1992; Blundy and Dalton 2000; Adam and Green 2001) support a link between these geochemical and modal features and carbonatite metasomatism. Heretic alternative interpretations showing that "carbonatite fingerprints" displayed by peridotite bulk-rock and minerals are not unequivocal indicators of carbonatite metasomatism have, however, been proposed by various Authors, who argue against the existence of a simple,

straightforward link between agent original composition and metasomatic consequence. For example, orthopyroxene dissolution, modal trend towards wehrlite and apatite crystallisation may be induced by any ne-normative silicate melt and especially nephelinites (Zinngrebe and Foley 1995; Xu et al. 1996; Neumann and Wulff-Pedersen 1997; Wulff-Pedersen et al. 1999; Peslier et al. 2002). REE-HFSE (high field strength elements) decoupling and LREE enrichment may be consistent with other agents, like hydrous silicate melts (Grégoire et al. 2001; Laurora et al. 2001; Bodinier et al. 2004). Elemental anomalies and fractionations may be process-dependent. In particular, infiltration processes accompanied by reactive porous flow may induce dramatic variations in the composition of the percolating metasomatic melt (Vernières et al. 1997; Bedini et al. 1997; Ionov et al. 2002; Bodinier et al. 2004), with consequent large variations of porosity, melt/rock ratios and element partition coefficients (Zinngrebe and Foley 1995; Bedini et al. 1997; Zanetti et al. 1999; Vannucci et al. 1998; Wulff-Pedersen et al. 1999) and, hence, of the metasomatic imprint. In such a process, the features of the metasomatic agent are recorded only in the mantle segment percolated by large melt volumes closer to the infiltration origin, but are soon lost by the reaction-induced variations (e.g. Ionov et al. 2002; Bodinier et al. 2004).

Since the controversy on carbonatite metasomatism may have important bearing for constraining the composition of the upper mantle and magma sources, we contribute to the discussion by revisiting a xenolith occurrence in the Patagonia backarc region, Gobernador Gregores. The xenoliths of this locality do display "carbonatite fingerprints", interpreted as induced either by carbonatite metasomatism (Gorring and Kay 2000) or by a hydrous silicate melt (Laurora et al. 2001). Considering the variations and mutual relationships of the carbonatite fingerprints, we re-enforce our doubts on the action of a carbonatite agent. Mineral name abbreviations are according to Kretz (1983).

Xenolith occurrence and petrography

Information on the geological framework and field characteristics of the Gobernador Gregores (GG) occurrence can be found in Gorring and Kay (2000, their *Lote 17* occurrence), Laurora et al. (2001) and Rivalenti et al. (2004). Xenoliths, up to 60 cm large, occur in pyroclastic deposits connected with the Pliocene post-plateau volcanism (Gorring and Kay 2001) ~400 km E of the actual Chile trench. The study of more than 200 xenoliths (Laurora et al. 2001) shows that lherzolite predominates (86%), followed by harzburgite (12%) and wehrlite-dunite (2%). All the Authors have distinguished the xenoliths into two main types, anhydrous and hydrous, on the basis of the absence or presence of amphibole ± phlogopite ± apatite. There is no clear textural distinction between the two groups, since most xenoliths have recrystallised granular or porphyroblastic texture. In the anhydrous group, however, olivine is often strained and clinopyroxene may have fine unmixing lamellae and abundant fluid inclusions, becoming thereby cloudy. In the hydrous group, pyroxenes are generally clear and unmixed. Laurora et al. (2001) emphasised that all the xenoliths contain veins and pockets of silicate glass, into which occur carbonate drops derived from liquid immiscibility (Chalot-Prat and Arnold 1999) and olivine, clinopyroxene and spinel ± Ti-oxides microphenocrysts. These glasses reacted with the peridotite matrix phases inducing, for example, spongy rims in clinopyroxene. Laurora et al. (2001) demonstrated that these veins and pockets were related to an essentially isochemical (except for CO_2 addition) decompression melting event of the hydrous metasomatic phases of the matrix and/or to infiltration of basalt. This occurred during xenolith transport in the basalt. These glasses, therefore, cannot be responsible for the pervasive metasomatic modifications documented in the GG xenoliths, not being of direct interest for the purposes of the present paper. However, the concentration of highly incompatible elements in bulk-rock may be biased by their presence, since these elements are highly concentrated in glasses.

Analytical methods

Major elements and Sc, V, Cr, and Ni in bulk-rock were analysed on pressed pellets by X-ray fluorescence spectrometry (XRF) at the "Dipartimento di Scienze della Terra dell'Università degli Studi di Modena e Reggio Emilia", Italy, using a Philips PW1480 XRF. The methods employed were those of Franzini et al. (1975) and Leoni and Saitta (1976). Analyses are considered accurate to within 2–5% and 10% for major and trace elements, respectively. Total iron was determined as FeO.

Sr, Y, Zr, Nb, Ba, REE, Hf, Ta, Th and U in bulk-rock were analysed by inductively coupled plasma–mass spectrometry (ICP-MS) at the Department of Earth Sciences of the Memorial University of Newfoundland, St. John's, NF, Canada. Full details of the procedure are given in Jenner et al. (1990). Detection limits are reported in Table 1. For quality control, two geological reference standards (gabbro CCRMP MRG-1 and basalt NIST SRM 688) were prepared and analysed with the samples, together with a reagent blank to measure the reagent contribution to the trace element values. Reagent blank concentrations were insignificant for all samples and have not been subtracted from sample concentrations. For most elements, the accuracy of the method (1 r.s.d.), determined from multiple analyses of the reference standards, is 3–7%.

Major element, Ti and Cr mineral analyses were carried out at the "Dipartimento di Scienze della Terra dell'Università degli Studi di Modena e Reggio Emilia", Italy, with an ARL-SEMQ electron microprobe in

Table 1 Bulk-rock major and trace element composition and mode of Gobernador Gregores xenoliths

Group		*1a*	*1a*	*1a*	*1a*	*1a*	*2a*	*2a*	*2a*	*2a*	*2a*	*2a*	*2a*	*1b*	*1b*	*2b*	*2b*	*2b*	*2b*	*2b*	*2b*	*2b*
Sample		GG25	GG54	GG71	GG79	GG118	GG28	GG36	GG49	GG50	GG69	GG73	GG58	GG4	GG78	GG30	GG92	GG113	GG65	GG106	GG33	GG86
Lithotype		Lh	Lh	Lh	Lh	Ha	Lh	Lh	Lh	Lh	Lh	Lh	We	Lh	Lh	Lh	Lh	Lh	Ha	Ha	We	We
(wt%)																						
SiO_2		41.72	45.07	43.97	43.06	44.70	44.23	43.36	43.22	44.17	42.74	44.09	41.50	43.48	41.51	43.25	42.05	44.01	42.46	43.55	41.31	41.62
TiO_2		0.02	0.03	0.05	0.05	0.01	0.12	0.03	0.06	0.11	0.04	0.02	0.06	0.10	0.22	0.05	0.38	0.07	0.05	0.04	0.12	0.07
Al_2O_3		1.05	1.48	1.81	2.02	0.54	3.03	1.36	1.75	2.67	1.33	1.11	2.22	1.37	2.18	1.19	2.66	1.37	1.24	1.19	1.34	1.15
FeO_{tot}		7.44	7.81	7.89	7.53	7.08	7.54	7.94	7.58	7.18	7.52	7.83	7.67	7.57	8.59	7.21	8.69	7.37	7.60	7.75	7.96	8.68
MnO		0.13	0.13	0.13	0.13	0.13	0.12	0.13	0.13	0.13	0.13	0.14	0.13	0.13	0.13	0.12	0.14	0.13	0.13	0.13	0.14	0.13
MgO		45.10	43.01	43.53	44.44	45.91	40.71	43.69	43.48	40.96	44.86	44.77	44.09	43.52	42.56	43.20	40.96	44.54	44.32	44.52	43.38	43.18
CaO		3.20	1.70	1.80	1.93	0.89	3.31	2.51	2.82	3.56	2.47	1.15	3.04	2.89	3.63	3.89	3.84	1.51	3.30	2.02	4.59	4.12
Na_2O		0.29	0.02	0.02	0.07	0.02	0.19	0.19	0.11	0.26	0.10	0.11	0.49	0.08	0.25	0.20	0.38	0.11	0.13	0.06	0.33	0.28
K_2O		0.03	0.00	0.00	0.00	0.00	0.01	0.04	0.01	0.03	0.04	0.03	0.07	0.03	0.02	0.03	0.14	0.01	0.03	0.02	0.05	0.07
P_2O_5		0.00	0.00	0.00	0.00	0.00	0.04	0.02	0.04	0.03	0.04	0.02	0.02	0.04	0.02	0.05	0.05	0.09	0.04	0.05	0.03	0.03
Cr_2O_3		0.74	0.45	0.51	0.49	0.39	0.42	0.44	0.51	0.63	0.44	0.44	0.42	0.47	0.61	0.51	0.46	0.48	0.39	0.35	0.46	0.37
NiO		0.28	0.30	0.28	0.28	0.33	0.27	0.29	0.30	0.27	0.29	0.29	0.30	0.31	0.28	0.30	0.27	0.29	0.30	0.31	0.30	0.30
Mg#		91.5	90.8	90.8	91.3	92.0	90.6	90.7	91.1	91.0	91.4	91.1	91.1	91.1	89.8	91.4	89.4	91.5	91.2	91.1	90.7	89.9
	Detection limit (ppm)																					
Sc	1	10	11	9	10	4	14	7	11	14	9	6	12	10	11	8	10	9	7	6	9	7
V	3	38	55	55	57	19	80	40	50	71	46	32	49	45	61	41	37	49	35	33	51	42
Ba	0.30	5.55	4.92	4.30	1.86	1.37	10.95	7.01	7.93	8.33	13.56	8.77	33.12	13.05	8.55	12.53	32.69	9.53	39.99	7.58	9.19	33.70
Sr	0.80	15.65	6.87	5.39	8.16	5.75	42.19	44.63	46.71	48.68	47.38	31.49	95.36	45.63	49.34	60.37	95.58	52.25	55.64	36.53	83.05	76.95
Ta	0.001	0.157	0.015	0.009	0.006	0.002	0.059	0.638	0.032	0.114	0.108	0.186	0.146	0.085	0.066	0.062	0.241	0.021	0.075	0.076	0.337	0.593
Nb	0.005	3.399	0.405	0.145	0.132	0.055	1.895	13.805	0.779	1.054	3.409	6.781	7.154	1.799	1.079	3.704	5.217	0.906	7.336	1.827	5.901	9.378
Hf	0.010	0.215	0.188	0.069	0.095	0.046	0.243	0.243	0.099	0.350	0.161	0.217	0.259	0.247	0.418	0.219	0.714	0.122	0.182	0.371	0.390	0.510
Zr	0.05	3.75	2.76	1.89	2.67	0.86	9.29	12.91	4.95	13.37	7.14	5.68	14.67	10.72	20.76	6.56	25.24	3.91	5.13	10.65	34.63	35.88
Y	0.015	0.686	0.775	0.915	1.582	0.114	3.510	1.790	1.602	2.254	1.310	1.404	3.761	1.311	2.761	1.384	2.957	1.376	1.517	1.197	2.828	2.604
Th	0.004	0.187	0.055	0.015	0.010	0.012	0.300	0.031	0.133	0.068	0.111	0.076	0.278	0.243	0.101	0.089	0.111	0.280	0.113	0.061	0.096	0.293
U	0.010	0.131	0.022	0.025	0.031	0.048	0.133	0.054	0.124	0.093	0.114	0.031	0.086	0.187	0.091	0.109	0.124	0.135	0.211	0.055	0.110	0.095
La	0.020	0.254	0.091	0.140	0.148	0.074	2.247	0.907	2.249	1.428	1.535	1.321	3.557	1.895	1.449	1.545	2.649	3.657	1.630	0.781	1.708	3.427
Ce	0.020	0.514	0.324	0.194	0.275	0.072	4.281	3.250	5.373	3.853	4.409	3.107	9.986	3.516	3.938	4.169	6.899	7.913	3.923	2.516	5.495	8.837
Pr	0.010	0.070	0.046	0.076	0.062	0.029	0.502	0.582	0.754	0.618	0.730	0.515	1.448	0.517	0.702	0.572	1.110	1.004	0.654	0.396	0.933	1.154
Nd	0.020	0.334	0.230	0.229	0.288	0.056	1.695	2.925	2.608	2.617	3.006	2.415	6.301	1.742	3.337	2.681	5.253	3.314	2.814	1.847	4.359	5.212
Sm	0.020	0.084	0.062	0.115	0.126	0.027	0.449	0.742	0.501	0.589	0.618	0.546	1.422	0.455	0.959	0.640	1.212	0.449	0.696	0.389	1.133	1.226
Eu	0.010	0.023	0.022	0.022	0.040	b.d.l.	0.105	0.235	0.091	0.153	0.135	0.168	0.444	0.097	0.315	0.188	0.399	0.082	0.150	0.099	0.354	0.372
Gd	0.020	0.096	0.087	0.111	0.178	0.011	0.445	0.597	0.289	0.482	0.417	0.475	1.177	0.303	0.898	0.455	1.029	0.254	0.481	0.292	0.952	1.075
Dy	0.010	0.114	0.121	0.149	0.254	0.016	0.585	0.425	0.268	0.403	0.269	0.320	0.879	0.272	0.653	0.319	0.729	0.213	0.322	0.203	0.669	0.698
Er	0.010	0.063	0.087	0.146	0.198	0.021	0.428	0.154	0.217	0.272	0.147	0.130	0.375	0.193	0.270	0.131	0.295	0.149	0.194	0.107	0.257	0.224
Yb	0.005	0.065	0.098	0.137	0.204	0.017	0.376	0.108	0.140	0.199	0.119	0.097	0.285	0.115	0.166	0.107	0.200	0.116	0.107	0.120	0.154	0.132
Mode (wt%)																						
Ol		70.7	61.7	61.8	66.8	74.0	52.3	68.7	53.6	63.7	72.1	70.1	79.5	68.8	79.8	64.1	59.0	67.3	77.4	71.5	79.6	79.4
Opx		13.5	30.7	29.1	23.1	22.3	34.9	20.1	33.2	20.5	18.5	22.4		22.2	6.7	22.5	20.1	25.0	11.5	21.6	1.9	1.7
Cpx		8.0	6.7	7.5	8.9	3.3	7.5	7.1	7.1	11.7	6.0	5.6	12.0	6.2	5.9	8.1	9.6	7.1	4.9	2.3	8.2	12.9
Sp		1.1	0.9	1.6	1.2	0.4	1.8	0.1	1.5	1.5	0.6	0.2	0.4	0.4	1.8	0.4	0.3	tr	0.2	tr	0.4	tr
Amph							2.5	2.7	2.8	1.1	1.0	1.7	8.1			1.5	8.7	0.6	4.2	2.6	6.7	3.9
Phlog									tr		0.5						0.3					
Glass		4.4	tr	tr	tr	tr	tr	tr	tr	tr		tr	tr	1.6	2.1	tr	tr	tr	tr	tr	tr	tr
Carb		2.3					1.0	1.3	1.8	1.5	1.3	tr	tr	0.8	3.7	3.5	2.0		1.8	2.0	3.2	2.1
Ap												tr			tr		tr	tr	tr			

tr trace, *bdl* below detection limit

wavelength dispersive mode, with an accelerating potential of 15 kV, a beam current of 20 nA, and a focused spot size of about 4 μm diameter. Natural minerals were used as standards. Counts were converted to weight percent oxides using the PROBE software by J.J. Donovan (Advanced Microbeam 4217 C, Kings Graces road, Vienna OH 44473, USA). Results are considered accurate within 2–6%.

Trace elements in pyroxenes and amphibole were analysed by laser-ablation (LA-ICP-MS) at the "CNR-Istituto di Geoscienze e Georisorse, Section of Pavia". The LA-ICP-MS is a double focussing sector field analyser (Finnigan Mat Element) coupled with a Q-switched Nd:YAG laser source (Quantel Brilliant), whose fundamental emission in the near-IR region (1,064 nm) is converted to 266 nm by two harmonic generators. Helium was used as carrier gas, mixed with Ar downstream of the ablation cell. Spot diameter was varied in the range 30–100 μm. NIST SRM 610 glass was used as external standards, with ^{44}Ca as internal standard for clinopyroxene and amphibole and ^{29}Si for orthopyroxene and phlogopite. Precision and accuracy, both better than 10% for concentrations at the ppm level, were assessed from repeated analyses of NIST SRM 612 and BCR-2g reference standards. Detection limits were typically in the range 100–500 ppb for Sc, 10–100 ppb for Sr, Zr, Ba, Gd and Pb, 1–10 ppb for Y, Nb, La, Ce, Nd, Sm, Eu, Dy, Er,Yb, Hf and Ta, and usually <1 ppb for Pr, Th and U.

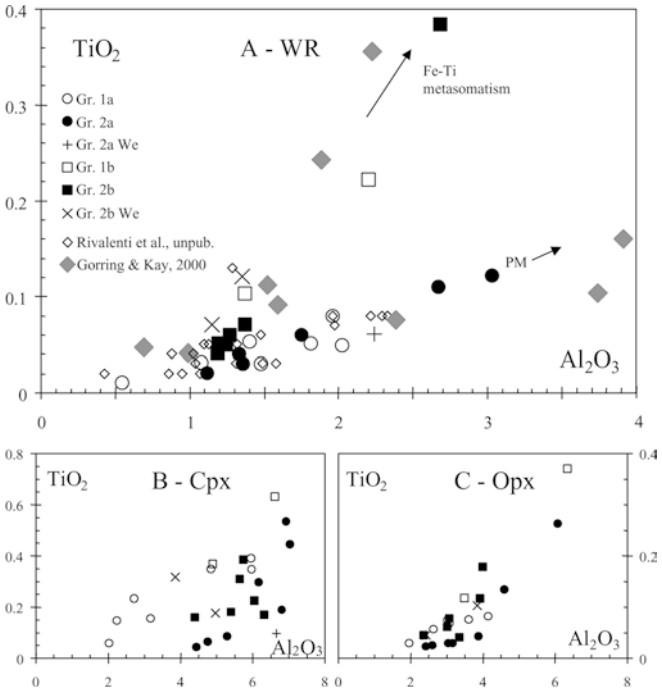

Fig. 1 **a** Variation of TiO_2 (wt%) vs. Al_2O_3 (wt%) in bulk-rock, distinguishing the present xenoliths into a HTi and a LTi array. Data from Gorring and Kay (2000) and our unpublished analyses are also reported. **b, c** Variation of TiO_2 (wt%) vs. Al_2O_3 (wt%) in clinopyroxene and orthopyroxene, respectively. The orthopyroxenes, and with a larger scatter also clinopyroxenes, of the HTi xenoliths have, at a given Al_2O_3, higher TiO_2 concentration than the phases in the LTi xenoliths, with the exception of the anhydrous LTi xenoliths (*circles*, see text)

Xenolith selection and grouping

The 26 samples selected for this study are representative of all the GG xenolith variety. Their modal composition, calculated by mass balance algorithms combining phase and whole rock major and trace elements composition, is reported in Table 1. Besides the obvious distinction in anhydrous (group 1) and hydrous (group 2) xenoliths, we add a further distinction based on the bulk rock TiO_2–Al_2O_3 variation trend. As shown in Fig. 1, samples split into two arrays, characterised by high (HTi) and low (LTi) Ti/Al respectively, merging at low TiO_2 and Al_2O_3 concentrations. The HTi array is on line with the host basalt and the LTi with the primitive mantle composition. This distinction is not a spurious effect induced by basalt infiltration, because it is reflected also in the core compositions of the silicate minerals and spinel (Tables 1, 2, 3, and 4 and Fig. 1 for pyroxenes). The HTi group consists both of anhydrous (cpx-poor lherzolites GG78 and GG4) and hydrous xenoliths (lherzolites GG30, GG92, GG26 and GG113; harzburgites GG65 and GG106; wehrlites GG33 and GG86). The LTi group consists of the rest of the anhydrous and hydrous groups and includes lherzolites, harzburgites and one wehrlite (GG58) (Table 1). The reason for distinguishing xenoliths by emphasising the Ti-Al relationships is that high Ti is considered an indicator of metasomatism operated by basaltic components (Menzies et al. 1987) and it is, therefore, important for the present issue. In summary, the groups used in the text are:

– Group *1a*, anhydrous LTi xenoliths
– Group *1b*, anhydrous HTi xenoliths
– Group *2a*, hydrous LTi xenoliths
– Group *2b*, hydrous HTi xenoliths.

Modal trends

Modal composition is reported in Table 1 and modal variation trends for the groups above distinguished are illustrated in Fig. 2, along with vectors indicating variations induced by melting or melt-peridotite mineralogical reactions. These comprise: (1) cpx formation by opx dissolution (wehrlite trend); (2) opx formation by ol ± cpx dissolution (harzburgite trend). Group *1a* xenoliths follow variation trends consistent with melting and basalt removal, discussed in detail in Rivalenti et al. (2004). Enough surprising, none of the *2a* xenoliths follows the wehrlite trend (with the obvious exception of the LTi wehrlite GG58), but rather fall in the harzburgite trend, with the highest opx concentrations (up to 35%) in lherzolites GG49 and GG28 of group *2a*. The

Table 2 Clinopyroxene major and trace element composition and olivine and spinel selected parameters of Gobernador Gregores xenoliths

Group	*1a*	*1a*	*1a*	*1a*	*1a*	*1a*	*1a*	*2a*	*2a*	*2a*	*2a*	*2a*	*2a*	*2a*	*2a*	*1b*	*1b*	*2b*	*2b*	*2b*	*2b*	*2b*	*2b*	*2b*	*2b*
Sample	GG31	GG54	GG71	GG79	GG85	GG112	GG118	GG28	GG36	GG49	GG50	GG104	GG69	GG73	GG58	GG4	GG78	GG26	GG30	GG92	GG113	GG65	GG106	GG33	GG86
Litho-type	Lh	Lh	Lh	Lh	Ha	Ha	Ha	Lh	Lh	Lh	Lh	Lh	Lh	Lh	We	Lh	Lh	Lh	Lh	Lh	Lh	Ha	Ha	We	We
(wt%)																									
SiO_2	52.81	53.00	53.54	53.00	53.53	52.43	54.03	53.87	53.73	52.63	52.61	53.90	52.65	53.25	53.42	52.59	52.68	53.03	54.43	53.38	53.38	53.88	53.73	53.57	54.16
TiO_2	0.39	0.15	0.23	0.35	0.15	0.35	0.06	0.19	0.09	0.53	0.45	0.04	0.30	0.07	0.10	0.37	0.63	0.39	0.16	0.23	0.31	0.18	0.17	0.32	0.18
Al_2O_3	5.96	3.18	2.73	5.97	2.24	4.84	2.02	6.81	5.29	6.92	7.03	4.45	6.15	4.76	6.65	4.89	6.61	5.74	4.39	6.04	5.63	5.40	6.31	3.85	4.96
FeO_{tot}	2.12	2.37	2.12	2.22	2.17	2.09	1.89	2.79	3.14	3.00	3.13	2.77	2.90	2.96	2.67	3.12	3.41	3.12	2.63	3.66	2.87	2.74	3.09	2.85	3.32
MnO	0.07	0.08	0.07	0.07	0.07	0.08	0.06	0.09	0.08	0.08	0.08	0.11	0.09	0.10	0.09	0.08	0.11	0.09	0.07	0.10	0.08	0.08	0.09	0.09	0.11
MgO	15.41	16.84	16.76	15.65	17.51	15.08	17.71	14.79	14.93	15.58	14.90	15.59	15.34	15.98	14.79	16.21	14.99	15.51	15.67	14.40	15.10	15.31	14.93	15.79	15.04
CaO	20.23	23.06	23.54	20.04	23.30	22.32	22.86	17.12	18.34	17.71	18.48	19.27	19.26	18.85	18.42	19.87	17.28	18.72	17.78	18.18	18.56	17.96	17.04	19.69	17.70
Na_2O	1.77	0.37	0.49	1.76	0.24	1.22	0.46	2.93	2.43	2.21	2.20	2.04	1.84	1.79	2.49	1.30	2.48	1.99	2.61	2.48	2.33	2.56	2.85	1.80	2.64
Cr_2O_3	1.21	0.93	0.49	0.90	0.77	1.56	0.87	1.38	1.94	1.30	1.10	1.78	1.46	2.21	1.33	1.53	1.76	1.38	2.23	1.53	1.70	1.84	1.74	2.02	1.86
Total	99.97	99.98	99.97	99.96	99.98	99.97	99.96	99.97	99.97	99.96	99.98	99.95	99.99	99.97	99.96	99.96	99.95	99.97	99.97	100.00	99.96	99.95	99.95	99.98	99.97
Mg#	92.8	92.7	93.4	92.6	93.5	92.8	94.4	90.4	89.4	90.2	89.5	90.9	90.4	90.6	90.8	90.2	88.7	89.9	91.4	87.5	90.4	90.9	89.6	90.8	89.0
(ppm)																									
Ba					0.859			0.055		0.193	0.047		0.985					5.453	1.085		0.745		1.160		0.072
Th	0.022	0.016		0.012	0.006	0.027	0.005	0.307	0.184	0.877	0.237	0.953	0.351	0.478	1.277	0.943	0.522	0.414	0.525	0.265	1.099	1.158	0.266	0.284	1.064
U	0.010	0.005		0.006	0.001	0.014	0.002	0.106	0.036	0.217	0.060	0.388	0.076	0.243	0.387	0.158	0.134	0.289	0.149	0.068	0.375	0.391	0.066	0.066	0.204
Nb	0.30	0.05		0.09		0.10		0.27	6.15	1.71	1.64	1.99	1.71	1.83	0.78	2.49	1.22	5.34	0.82	0.49	0.33	1.90	0.97	2.62	2.81
Ta	0.050					0.032		0.012	0.604	0.096	0.484	0.238	0.052	0.113	0.100	0.200	0.157	0.761		0.155		0.056	0.104	0.553	0.363
La	1.07	0.45	0.28	0.62	0.11	1.15	0.06	11.85	8.43	19.30	7.24	15.94	16.82	12.99	18.76	10.81	8.74	9.63	14.09	12.70	27.43	16.74	9.56	10.29	18.34
Ce	3.87	1.76	1.06	1.99	0.37	2.98	0.13	38.81	32.25	54.41	29.81	48.73	62.63	44.44	54.04	20.84	25.80	27.26	40.43	47.30	95.23	43.80	46.16	36.04	48.33
Pr	0.73	0.32	0.22	0.38	0.07	0.56	0.03	5.65	6.15	6.77	4.52	6.77	9.07	6.49	7.24	2.41	4.48	3.90	6.41	7.24	10.68	6.66	7.97	5.96	6.44
Sr	82.1	22.7	15.2	41.0	7.7	51.2	7.5	307.0	327.1	367.7	272.5	385.7	497.6	384.2	383.4	227.7	258.9	264.7	381.1	333.2	453.3	373.4	359.2	348.4	344.3
Nd	4.40	1.85	1.47	2.30	0.42	3.45	0.37	22.99	33.21	24.33	19.25	28.96	39.02	30.17	30.75	9.96	23.95	17.47	30.64	30.91	35.80	31.06	37.38	30.68	27.09
Zr	19.4	5.1	6.6	12.5	1.7	21.5	3.2	27.6	88.4	27.8	67.0	63.2	19.1	30.2	49.4	29.8	135.3	53.1	35.3	89.7	23.3	33.3	101.1	225.4	146.0
Hf	0.67	0.18	0.34	0.45	0.16	0.78	0.08	0.74	0.53	0.65	1.57	0.18	0.15	0.10	0.67	0.89	1.61	1.28	0.79	2.27	0.95	1.13	2.65	1.74	1.10
Sm	1.53	0.56	0.63	0.95	0.18	1.26	0.24	5.30	9.21	4.88	4.88	6.87	8.21	7.67	7.68	2.57	7.60	4.53	7.78	8.32	6.50	8.09	8.92	7.76	7.16
Eu	0.58	0.19	0.28	0.44		0.48		1.51	3.06	1.32	1.49	1.84	2.08	2.20	2.29	0.95	2.46	1.19	2.24	2.32	1.39	2.32	2.29	2.31	2.18
Gd	1.88	0.60	0.98	1.71	0.37	1.56		4.03	7.71	3.44	3.74	4.48	4.42	5.13	5.96	2.22	6.36	3.39	5.93	5.13	3.08	6.36	5.47	5.99	5.97
Dy	2.33	0.72	1.22	2.23	0.48	1.88	0.51	2.90	4.95	2.69	2.92	2.83	2.66	3.36	3.99	2.21	4.46	2.73	3.74	3.78	2.62	4.33	3.74	4.48	3.69
Y	12.2	4.3	6.8	12.3	2.8	10.4	2.4	14.9	16.2	14.8	14.9	11.7	11.5	13.1	16.7	8.8	13.5	12.1	13.9	13.9	12.1	16.2	15.4	13.2	16.3
Er	1.51	0.46	0.82	1.56	0.44	1.15	0.29	1.34	1.66	1.39	1.51	1.27	1.04	1.26	1.69	0.96	1.38	1.06	1.55	1.63	1.38	1.59	1.49	1.37	1.21
Yb	1.48	0.49	0.89	1.54	0.48	1.30	0.34	1.19	0.74	1.23	1.33	1.17	0.84	0.92	1.51	0.81	0.75	1.09	1.14	1.11	1.15	1.17	1.36	0.92	0.72
Sc	56.8	56.2	54.9	59.4	50.8	68.2	61.6	63.4	56.0	60.5	58.4	54.4	67.3	63.2	55.4	50.6	61.3	60.9	70.4	60.8	66.4	62.9	57.1	58.0	46.7
T (°C)	987	891	754	1,014	887	774	917	1,118	1,067	1,109	1,094	1,039	1,073	1,108		1,090	1,135	1,094	1,103	1,053	1,071	1,091	1,131	1,029	1,100
P (GPa)	2.3	2.8	0.4	1.9	2.5	1.1	2.2	2.6	0.7	1.3	2.0	1.3	1.6	3.0		1.1	0.6	1.3	2.4	1.0	1.8	0.5	2.8	0.5	

Blanck values below detection limit (see text), *T* Brey and Köhler (1990), *P* Köhler and Brey (1990)

Table 3 Orthopyroxene major and trace element composition of Gobernador Gregores xenoliths

Group	*1a*	*1a*	*1a*	*1a*	*1a*	*1a*	*1a*	*2a*	*2a*	*2a*	*2a*	*2a*	*2a*	*2a*	*1b*	*1b*	*2b*	*2b*	*2b*	*2b*	*2b*	*2b*	*2b*
Sample	GG31	GG54	GG71	GG79	GG85	GG112	GG118	GG28	GG36	GG49	GG50	GG104	GG69	GG73	GG4	GG78	GG30	GG92	GG113	GG65	GG106	GG33	GG86
Lithotype	Lh	Lh	Lh	Lh	Ha	Ha	Ha	Lh	Lh	Lh	Lh	Lh	Lh	Lh	Lh	Lh	Lh	Lh	Lh	Ha	Ha	We	We
(wt%)																							
SiO_2	55.75	55.78	55.94	55.33	56.04	55.93	56.76	55.43	55.67	53.54	55.01	56.14	55.92	56.25	55.53	53.53	56.37	54.86	55.91	55.77	55.73	55.36	56.25
TiO_2	0.08	0.07	0.06	0.08	0.06	0.07	0.03	0.04	0.03	0.26	0.14	0.03	0.03	0.02	0.12	0.37	0.05	0.18	0.08	0.06	0.04	0.10	0.04
Al_2O_3	3.60	3.07	3.03	4.14	2.63	3.03	1.96	3.88	3.15	6.07	4.59	2.61	3.03	2.42	3.49	6.34	2.36	3.99	3.07	3.01	3.35	3.84	2.42
FeO_{tot}	5.54	6.11	6.53	5.73	6.51	5.57	5.23	6.09	6.48	8.55	5.92	6.06	5.83	5.91	5.64	6.92	5.83	7.99	5.67	6.08	6.11	6.09	6.14
MnO	0.14	0.15	0.16	0.13	0.15	0.13	0.14	0.14	0.15	0.15	0.14	0.14	0.14	0.16	0.14	0.16	0.14	0.15	0.13	0.11	0.13	0.14	0.16
MgO	33.91	33.72	33.54	33.19	33.70	34.04	34.80	32.99	32.80	30.38	32.62	33.59	33.48	33.78	33.25	30.82	33.58	31.45	33.58	33.44	32.95	32.82	33.52
CaO	0.50	0.61	0.33	0.77	0.41	0.63	0.51	0.66	0.85	0.80	0.85	0.70	0.74	0.63	0.94	1.16	0.73	0.84	0.70	0.66	0.73	0.90	0.73
Na_2 O	0.06	0.01	0.05	0.13	0.03	0.05	0.04	0.18	0.16	0.16	0.20	0.13	0.15	0.13	0.12	0.25	0.21	0.19	0.17	0.16	0.26	0.18	0.18
Cr_2O_3	0.40	0.43	0.35	0.45	0.44	0.50	0.50	0.53	0.68	0.04	0.48	0.56	0.64	0.65	0.73	0.42	0.69	0.31	0.65	0.63	0.64	0.53	0.49
Total	99.98	99.95	99.99	99.95	99.97	99.95	99.97	99.94	99.97	99.95	99.95	99.96	99.96	99.95	99.96	99.97	99.96	99.96	99.96	99.92	99.94	99.96	99.93
Mg#	91.6	90.8	90.1	91.2	90.2	91.6	92.2	90.6	90.0	86.4	90.8	90.8	91.1	91.1	91.3	88.8	91.1	87.5	91.3	90.7	90.6	90.6	90.7
(ppm)																							
Ba								0.027		0.050	0.025												
Th		0.005		0.002		0.001	0.025	0.002		0.005	0.003	0.013				0.025		0.004	0.007	0.006	0.001	0.003	0.007
U		0.002	0.003				0.043	0.002				0.012		0.003		0.013	0.002	0.002	0.012	0.010			0.001
Nb								0.017	0.169	0.039	0.076		0.065			0.028					0.050	0.160	0.103
Ta								0.003			0.009											0.037	0.005
La								0.020		0.020	0.016					0.147			0.052		0.037	0.098	0.036
Ce				0.007		0.007		0.118	0.068	0.125	0.107	0.077	0.165	0.072		0.369	0.065	0.118	0.219	0.132	0.169	0.378	0.148
Pr								0.024		0.025	0.022		0.033			0.045		0.024	0.041		0.035	0.078	0.030
Sr								0.822	0.732	0.762	0.748	0.574	0.851	0.642		3.200	0.555	0.718	1.073	0.603	0.893	3.365	0.994
Nd						0.020		0.131	0.135	0.112	0.133	0.118	0.235			0.295	0.088	0.148	0.221	0.173	0.203	0.446	0.187
Zr		0.342	0.504	0.394	0.236	0.535		1.045	3.094	1.173	3.990	1.775	1.148	0.775		3.590	0.668	5.773	0.964	0.792	3.925	10.135	3.963
Hf			0.039	0.041	0.010	0.016		0.022		0.036	0.101					0.055		0.119	0.040	0.071	0.075	0.193	0.027
Sm						0.008		0.051			0.049		0.106	0.032		0.125			0.062		0.073		0.075
Eu								0.021			0.030		0.054			0.055			0.016			0.057	0.031
Gd								0.088			0.090		0.227										0.113
Dy	0.003		0.051	0.058		0.045		0.124	0.125	0.086	0.124	0.065	0.178	0.108	0.004		0.124	0.143	0.107	0.132	0.129	0.216	0.155
Y		0.284	0.428	0.513	0.156	0.379		0.848	0.814	0.912	1.010	0.541	0.672	0.666		0.983	0.471	0.830	0.789	0.687	0.848	1.005	0.957
Er		0.084	0.077	0.078	0.044	0.063		0.102		0.109	0.113		0.089			0.163	0.113	0.086	0.111	0.045	0.116	0.082	0.095
Yb		0.164	0.150	0.150	0.100	0.138		0.159	0.173	0.147	0.156	0.183	0.125				0.081	0.147	0.175		0.142		0.101
Sc	3.5	19.1	14.6	12.5	20.7	15.2	41.6	14.0	8.8	14.5	15.2	7.2	13.5	7.8	3.5	6.8	9.9	8.8	14.9	10.5	11.7	14.5	8.1

Blanck values below detection limit (see text)

Table 4 Amphibole major and trace element composition of Gobernador Gregores xenoliths

Group	*2a*	*2a*	*2a*	*2a*	*2a*	*2a*	*2a*	*2a*	*2b*	*2b*	*2b*	*2b*	*2b*	*2b*
Sample	GG28	GG36	GG49	GG50	GG104	GG69	GG73	GG58	GG30	GG92	GG65	GG106	GG33	GG86
Lithotype	Lh	Lh	Lh	Lh	Lh	Lh	Lh	We	Lh	Lh	Ha	Ha	We	We
(wt%)														
SiO_2	43.62	44.42	42.67	42.78	43.37	43.63	44.53	42.49	44.08	42.93	43.96	43.67	43.78	43.40
TiO_2	1.12	0.61	2.52	2.32	0.37	1.10	0.34	0.61	0.92	3.40	1.10	1.47	3.91	1.12
Al_2O_3	15.46	13.98	14.00	15.08	13.63	14.76	13.32	15.19	13.06	14.29	14.08	14.32	13.99	13.83
FeO_{tot}	3.87	3.91	3.78	4.07	3.60	3.84	3.76	3.70	3.64	5.57	3.57	3.74	4.32	4.07
MnO	0.06	0.06	0.06	0.07	0.06	0.05	0.07	0.06	0.06	0.06	0.05	0.04	0.07	0.06
MgO	17.33	17.77	17.93	17.02	18.48	17.76	18.26	18.45	18.83	16.10	17.95	17.63	16.43	18.53
CaO	9.32	9.62	10.39	9.99	10.93	9.87	10.21	10.46	9.36	9.66	9.72	9.58	9.06	9.36
Na_2O	4.20	3.77	3.26	3.34	3.46	3.41	3.48	4.14	3.97	3.43	3.75	4.01	3.59	3.94
K_2O	0.97	1.62	1.80	1.72	1.50	1.65	1.28	1.03	1.13	1.67	1.22	1.01	1.25	1.37
Cr_2O_3	1.83	2.10	1.49	1.41	2.44	1.78	2.57	1.77	2.70	0.78	2.40	2.40	1.49	2.12
Cl		0.03			0.07	0.04	0.08			0.02	0.12	0.02	0.02	
Total	97.78	97.89	97.90	97.80	97.91	97.89	97.90	97.90	97.75	97.91	97.92	97.89	97.91	97.80
Mg#	88.9	89.0	89.4	88.2	90.1	89.2	89.6	89.9	90.2	83.7	90.0	89.4	87.1	89.0
(ppm)														
Rb	2.8	2.2	7.6	4.5	5.5	2.9	4.9	5.3	3.6	5.9	3.1	4.5	3.3	2.4
Ba	112	51	281	120	427	103	204	421	224	222	460	135	125	148
Th	0.28	0.052	0.73	0.15	1.2	0.20	0.57	1.4	0.59	0.22	0.96	0.24	0.066	1.6
U	0.11	0.022	0.22	0.046	0.40	0.075	0.25	0.33	0.19	0.066	0.33	0.054	0.050	0.36
Nb	24	375	160	69	295	248	250	73	81	23	166	57	40	230
Ta	0.27	19	5.0	5.2	10	4.4	4.8	1.3	1.4	1.2	1.2	1.5	2.1	13
La	13.4	7.3	18.7	7.8	22.8	15.2	17.8	22.9	17.2	9.2	17.1	12.3	4.8	24.0
Ce	43.0	30.7	59.6	30.2	64.9	65.4	58.2	61.7	42.6	32.7	44.3	54.6	16.9	53.0
Pb	0.64	0.51	0.86	0.50	1.2	0.58	1.4	1.5	1.4	0.59	1.1	0.56	0.55	0.57
Pr	6.1	5.7	7.9	4.6	9.0	11.3	8.9	8.4	5.7	5.3	6.5	8.8	3.4	6.9
Sr	562	559	805	659	659	901	667	649	566	612	638	678	531	512
Nd	24.6	31.9	30.1	20.8	36.5	50.0	37.4	33.9	24.6	24.4	29.0	39.2	20.3	29.4
Zr	26	111	50	82	81	77	44	53	36	83	33	50	68	161
Hf	0.66	1.1	1.0	1.8	0.18	1.7	0.21	0.49	0.78	2.2	0.97	1.4	1.6	1.2
Sm	5.8	9.3	6.8	5.5	8.8	12.6	10.0	8.2	6.5	7.0	7.9	9.4	6.9	7.6
Eu	1.64	3.1	1.79	1.65	2.30	3.1	2.60	2.23	2.09	2.08	2.32	2.50	2.21	2.20
Gd	4.0	7.8	4.8	4.1	5.0	6.5	5.4	5.6	5.3	5.0	6.3	5.6	5.8	5.7
Dy	2.89	4.4	3.2	2.70	2.95	3.6	3.5	3.9	3.3	2.92	4.1	3.3	3.7	3.4
Y	13.8	14.6	16.2	13.7	12.4	12.8	14.5	16.6	12.2	12.3	14.7	14.9	13.2	13.2
Er	1.30	1.35	1.48	1.15	1.16	1.28	1.42	1.66	1.17	1.09	1.33	1.41	1.25	1.04
Yb	1.10	0.88	1.16	0.98	0.88	1.11	0.98	1.41	0.86	0.74	1.09	1.22	0.81	0.58
Sc	36	32	43	37	37	37	46	36	39	26	35	36	22	26

Blanck values below detection limit (see text)

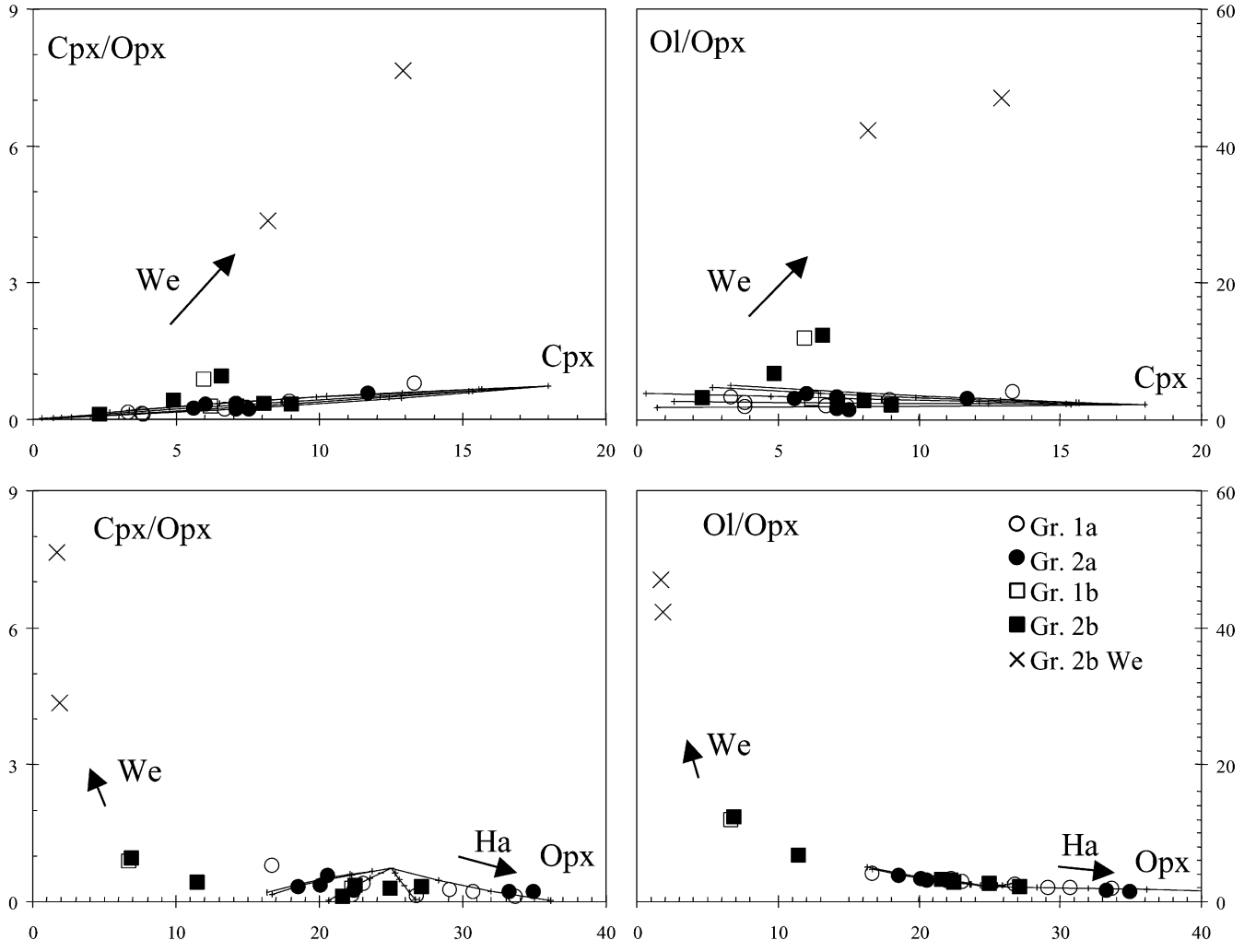

Fig. 2 Variation of the modal ratios cpx/opx and ol/opx versus modal cpx and opx. *Thin lines* are model variation trends induced by anhydrous (Baker and Stolper 1994; Kinzler 1997, at 1.9 GPa) and hydrous (Hirose and Kawamoto 1995; Gaetani and Grove 1998, at 1.2 GPa) melting on a mantle having the mode reported by Johnson et al. (1990). The *arrows* are qualitative vectors of reactions dissolving olivine and forming opx (*Ha* harzburgite trend) and dissolving opx and forming ol and cpx (*We* wehrlite trend)

wehrlite trend is followed only by HTi xenoliths. These trends are qualitatively maintained if cpx + amph, instead of only cpx, is used.

Analytical results

Analytical data on bulk rock and mineral phases are reported in Tables 1, 2, 3, 4 and 5. Information on phlogopite and apatite is reported in Laurora et al. (2001). In order to minimise the geochemical variations induced by reaction with glass, mineral analyses refer exclusively to core compositions, because analyses across the crystals revealed that element diffusion affected the rims, but not the inner portion of the crystals. Because of the glass presence, in the following description we also preferentially emphasise pyroxene and amphibole rather than bulk-rock characteristics.

Major elements -The most refractory compositions occur in group *1a* that has the most forsteritic olivine (Fo 91.9 in GG118, Table 5), the highest Mg# values [MgO/(MgO + FeO_{tot}) in moles] and the lowest Na_2O concentration in bulk-rock and mineral phases. Bulk-rock, clinopyroxene and amphibole of groups *1b, 2a* and *2b* have comparatively high Na_2O concentrations and low Mg# values (especially in group *2b*: e.g. Mg# is 89.4–89.9 in bulk-rock and 87.5–89.0 in cpx of samples GG92 and GG86, respectively, Tables 1 and 2). The TiO_2 enrichment with respect to Al_2O_3 observed in the bulk-rock composition of the *b* groups corresponds with a complementary Ti enrichment in clinopyroxene (Table 2), orthopyroxene (Table 3) and spinel (Table 5). In amphibole (pargasite to titanian pargasite; Table 4), the highest TiO_2 concentrations occur in the group *2b* samples GG92 and GG33 (TiO_2 = 3.40 and 3.91 wt%, respectively). Anyway, the other *2a* and *2b* amphiboles have a similar TiO_2 range. The CaO/Al_2O_3 and Na_2O/Al_2O_3 values in the *1a* xenoliths are higher than those of

Table 5 Olivine and spinel major element composition of Gobernador Gregores xenoliths

Group	*1a*	*1a*	*1a*	*1a*	*1a*	*1a*	*1a*	*1a*	*2a*	*2a*	*2a*	*2a*	*2a*	*2a*	*2a*	*2a*	*1b*	*1b*	*2b*	*2b*	*2b*	*2b*	*2b*	*2b*	*2b*
Sample	GG25	GG31	GG54	GG71	GG79	GG85	GG112	GG118	GG28	GG36	GG49	GG50	GG104	GG69	GG73	GG58	GG4	GG78	GG26	GG30	GG92	GG113	GG65	GG106	GG33	GG86
Litho-type	Lh	Lh	Lh	Lh	Lh	Ha	Ha	Ha	Lh	Lh	Lh	Lh	Lh	Lh	Lh	We	Lh	Lh	Lh	Lh	Lh	Lh	Ha	Ha	We	We
Olivine (wt%)																										
SiO_2	40.90	40.92	40.84	40.79	40.85	40.86	40.93	41.14	40.79	40.82	41.00	41.02	40.87	40.95	40.87	40.80	40.90	40.84	40.86	40.92	40.49	40.95	40.98	40.93	40.83	40.68
TiO_2	0.01	0.01	0.00	0.00	0.01	0.01	0.01	0.00	0.00	0.00	0.01	0.00	0.01	0.01	0.01	0.01	0.00	0.02	0.00	0.00	0.02	0.00	0.01	0.00	0.01	0.01
FeO_{tot}	9.01	8.88	9.39	9.54	9.29	9.20	8.83	7.89	9.55	9.42	8.53	8.40	9.20	8.68	9.16	9.55	8.92	9.29	9.18	8.84	11.15	8.75	8.47	8.83	9.27	10.14
MnO	0.12	0.13	0.12	0.13	0.11	0.13	0.12	0.13	0.13	0.13	0.10	0.12	0.14	0.14	0.13	0.15	0.13	0.14	0.12	0.14	0.14	0.12	0.14	0.13	0.15	0.16
MgO	49.50	49.60	49.19	49.05	49.23	49.32	49.61	50.31	49.02	49.04	49.81	49.94	49.30	49.69	49.32	48.99	49.42	49.03	49.23	49.59	47.67	49.63	49.69	49.55	49.19	48.54
CaO	0.04	0.04	0.02	0.03	0.05	0.03	0.02	0.03	0.06	0.10	0.10	0.07	0.07	0.07	0.05	0.06	0.11	0.15	0.09	0.06	0.08	0.06	0.12	0.06	0.09	0.06
Cr_2O_3	0.02	0.02	0.00	0.02	0.01	0.01	0.03	0.02	0.03	0.03	0.06	0.02	0.02	0.05	0.04	0.03	0.06	0.04	0.03	0.02	0.01	0.02	0.04	0.04	0.03	0.01
NiO	0.38	0.39	0.40	0.41	0.41	0.42	0.42	0.44	0.40	0.43	0.36	0.39	0.38	0.39	0.37	0.39	0.42	0.35	0.38	0.41	0.41	0.40	0.42	0.44	0.39	0.38
Total	99.98	99.99	99.96	99.97	99.96	99.98	99.97	99.96	99.98	99.97	99.97	99.96	99.99	99.98	99.95	99.98	99.96	99.86	99.89	99.98	99.97	99.93	99.87	99.98	99.96	99.98
Fo%	90.7	90.9	90.3	90.2	90.4	90.5	90.9	91.9	90.1	90.3	91.2	91.4	90.5	91.1	90.6	90.1	90.8	90.4	90.5	90.9	88.4	91.0	91.3	90.9	90.4	89.5
Spinel (wt%)																										
TiO_2	0.08	0.11	0.06	0.07	0.07	0.12	0.13	0.05	0.11	0.08	0.27	0.22	0.10	0.18	0.06		0.47	0.56	0.32		0.46	0.26	0.16	0.11	0.78	
Al_2O_3	6.67	52.59	45.73	50.74	55.09	41.77	44.92	29.22	42.88	34.72	47.04	51.64	33.20	37.51	28.70		34.81	46.83	42.98		43.78	38.09	36.35	36.02	32.95	
FeO_{tot}	23.13	10.22	14.55	13.03	10.10	16.12	12.16	16.10	13.70	15.61	12.21	12.40	14.67	14.65	16.07		15.64	14.63	14.05		17.76	13.98	13.86	14.77	16.97	
MnO	0.30	0.11	0.16	0.12	0.11	0.17	0.15	0.20	0.14	0.17	0.11	0.12	0.21	0.16	0.22		0.12	0.16	0.16		0.18	0.15	0.20	0.15	0.23	
MgO	12.96	21.46	17.49	19.21	21.62	16.05	19.32	15.02	19.63	16.90	20.49	19.49	17.10	17.76	15.34		16.97	18.08	18.44		17.19	17.89	17.52	16.36	16.82	
CaO	0.06	0.01	0.01	0.02	0.01	0.01	0.01	0.02	0.01	0.03	0.01	0.01	0.02	0.02	0.01		0.02	0.02	0.02		0.02	0.00	0.03	0.01	0.01	
Cr_2O_3	57.23	15.05	21.96	16.59	12.79	25.76	23.29	39.56	23.13	32.41	19.47	15.67	34.73	29.67	39.78		31.84	19.56	23.94		20.61	29.57	31.96	32.51	32.41	
NiO	0.14	0.36	0.30	0.33	0.34	0.23	0.26	0.15	0.34	0.28	0.34	0.37	0.24	0.27	0.19		0.26	0.33	0.31		0.31	0.30	0.24	0.29	0.23	
Total	100.57	99.91	100.26	100.11	100.13	100.23	100.24	100.32	99.94	100.20	99.94	99.92	100.27	100.22	100.37		100.13	100.17	100.22		100.31	100.24	100.32	100.22	100.40	
Mg#	50.0	78.9	68.2	72.4	79.2	64.0	73.9	62.4	71.9	65.9	74.9	73.7	67.5	68.4	63.0		65.9	68.8	70.0		63.3	69.5	69.3	66.4	63.8	
Cr#	85.2	16.1	24.4	18.0	13.5	29.3	25.8	47.6	26.6	38.5	21.7	16.9	41.2	34.7	48.2		38.0	21.9	27.2		24.0	34.2	37.1	37.7	39.7	

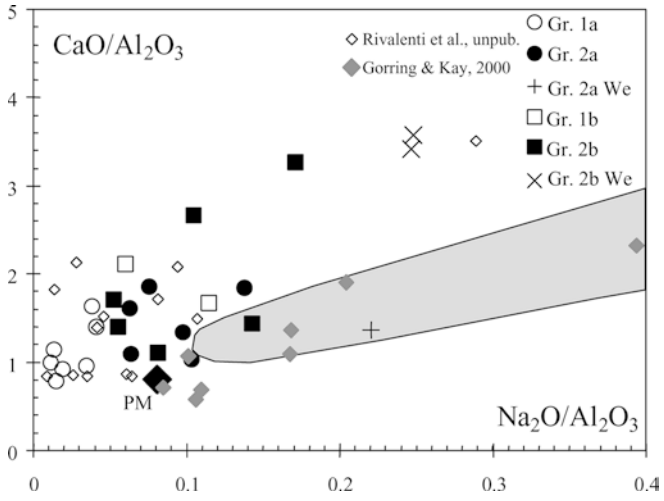

Fig. 3 Bulk-rock variation of CaO/Al_2O_3 vs. Na_2O/Al_2O_3, compared with the variation in the Southeastern Australia xenoliths (shaded field, Yaxley and Green 1996). Data from Gorring and Kay (2000) and our unpublished analyses are also reported. *PM* primitive mantle (Hofmann 1988)

Fig. 4 Primitive mantle (Hofmann 1988)-normalised trace element bulk-rock profiles for the four xenolith groups and wehrlites. *Continuous lines* lherzolites, *dashed lines* harzburgites and cpx-poor lherzolites. The *lines labelled 5*, *10*, *15* and *20* are model residues of 5–20% fractional melting of a PM source (Hofmann 1988). Melting parameters: initial and melting modes = Johnson et al. (1990) and Gaetani and Grove (1998) experiment 38–41, respectively. Partition coefficients: Ionov et al. (2002) for ol, opx and sp; Hart and Dunn (1993) for cpx. Melting equation = Shaw (1970)

PM (0.79 and 0.08, respectively) (Fig. 3). The values of these parameters are even higher in the other three groups.

REE -In agreement with their major element depleted composition, the *1a* xenoliths have bulk-rock REE concentration below 0.3xPM (Primitive Mantle, Hofmann 1988) and flat or slight LREE-enriched or depleted REE pattern (Fig. 4). The *1a* cpx have predominantly LREE-depleted patterns, nearly flat from Sm to Yb, whereas the *1b, 2b* and *2a* clinopyroxenes have LREE-enriched patterns resembling those of peridotites affected by alkali-basalt metasomatism (Fig. 5). The REE concentrations and patterns are similar in amphiboles and coexisting clinopyroxenes (compare Figs. 5 and 7a–c). The LREE concentration in the *1a* opx is below the detection limit (Table 3, Fig. 6). Although LREE-depleted, the *1b, 2b* and *2a* orthopyroxenes have relatively high Ce_n/Yb_n values (0.10–0.34 and 0.21–0.33 in groups *2a* and *2b*, respectively) (Fig. 6). Although harzburgites may have lower bulk-rock and phase REE concentrations, their variation range largely overlaps that of lherzolites. Wehrlites have REE concentrations in the range of the group they belong to.

Zr, Hf and Ti -The clinopyroxenes of group *1a* have low concentrations of Zr, Hf and Ti, which are slightly depleted with respect to L-MREE. Clinopyroxenes and amphiboles from groups *2a, 1b* and *2b* show very vari-

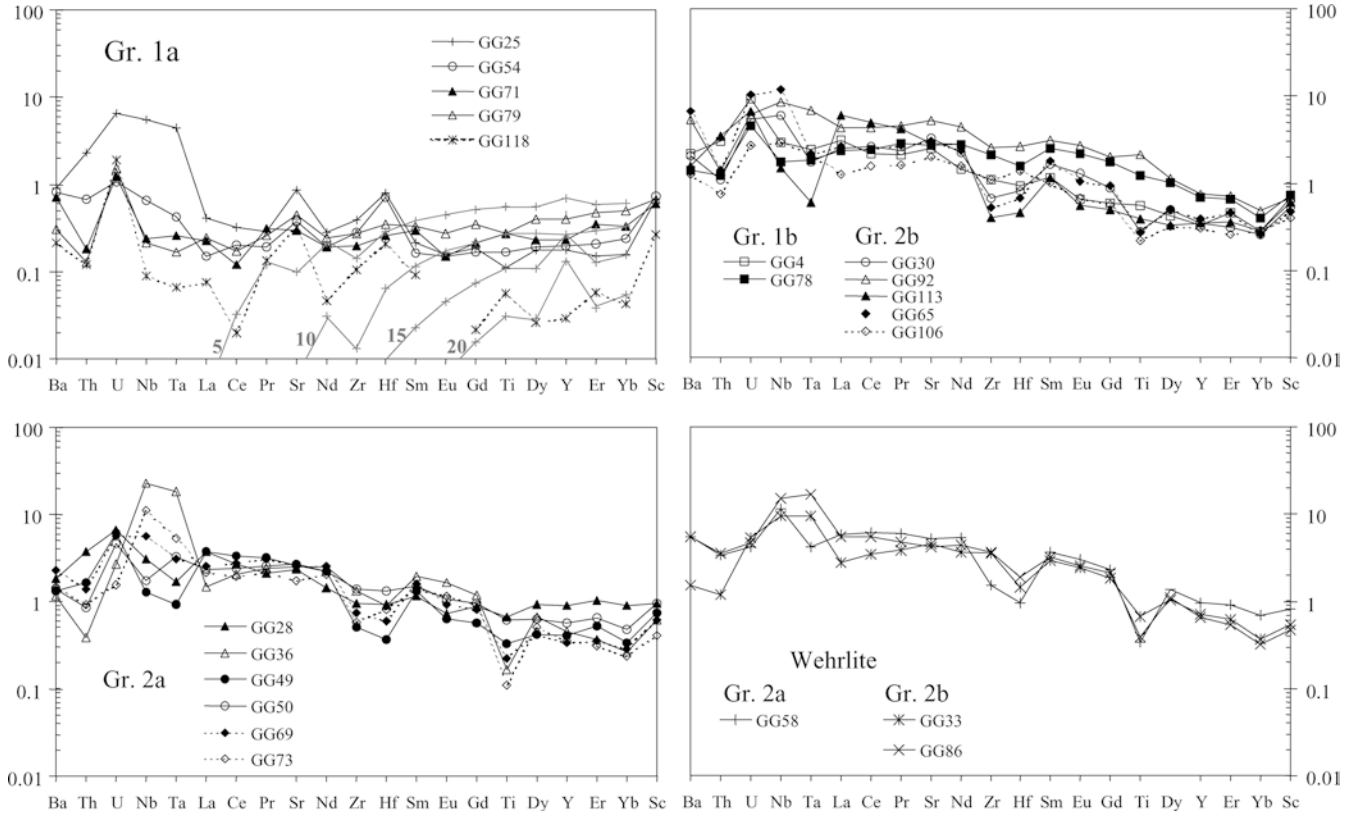

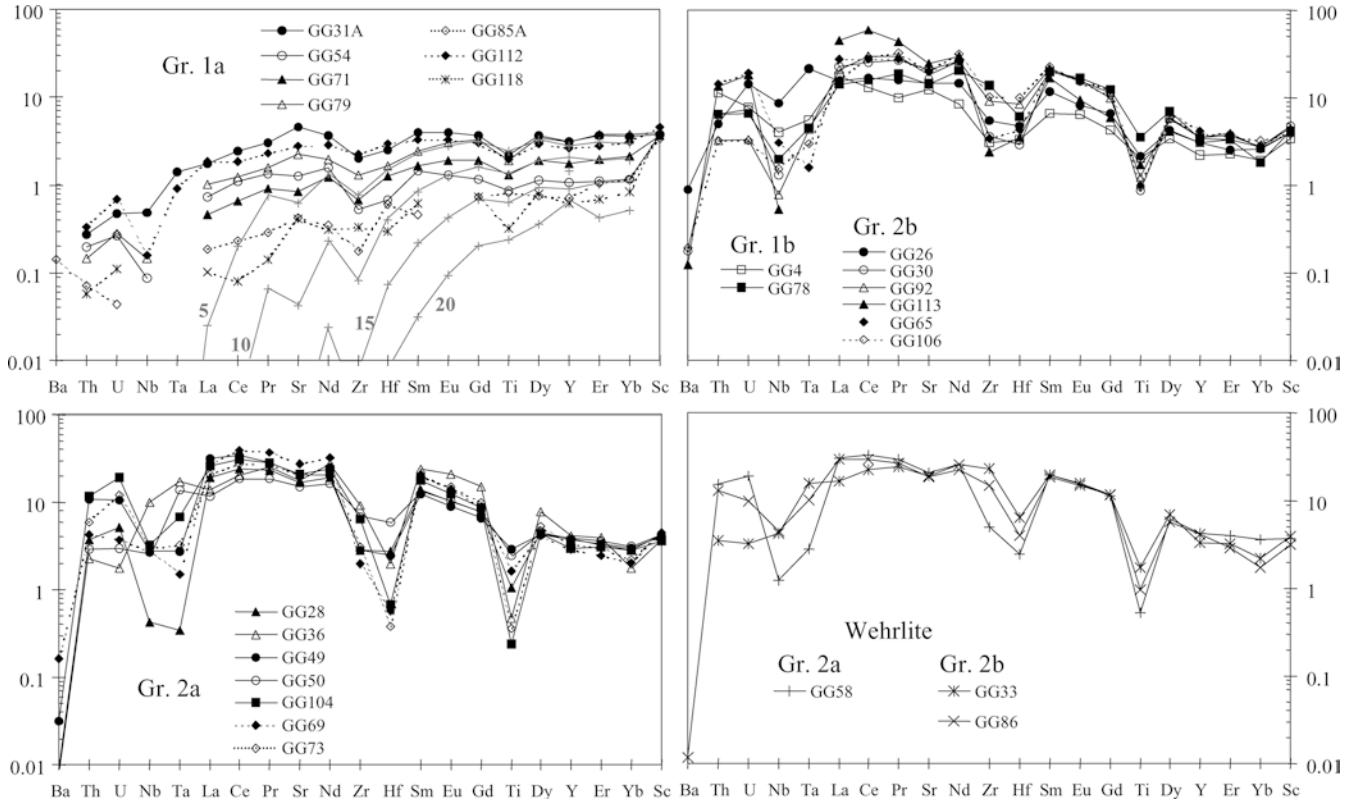

Fig. 5 Primitive mantle (Hofmann 1988)-normalised trace element profiles of clinopyroxenes in the four xenolith groups and wehrlites. The *lines labelled 5*, *10*, *15* and *20* are model residues of 5–20% fractional melting of a PM source (Hofmann 1988). Melting parameters as in Fig. 4

able amounts of Zr and Hf, which are moderately to extremely (e.g. GG73) depleted with respect to L-MREE (Figs. 5 and 7a-c). Most amphiboles and pyroxenes have Zr/Hf = 35–40 and define a trend close to the PM value, whereas the rest (HTi and LTi wherlites and the four LTi samples having the most pronounced negative Ti and Hf anomalies) lie in a field of relative Hf depletion (Zr/Hf value > 100) (Fig. 8a). Ti behaves like Zr and Hf, but it exhibits a positive spike in some group *2b* amphiboles (Fig. 7a-c), according to the well-documented (e.g. Vannucci et al. 1995) larger capability of this mineral to host Ti with respect to pyroxenes and olivine. This also explains the occurrence of a positive Ti spike in bulk-rock pattern of *2b* GG92 sample. Figure 8b illustrates the positive correlation between Gd_n/Ti_n and Nd_n/Hf_n ratios in cpx and amph. Bulk rock would provide results similar to cpx, only with a larger point spread because of the glass presence. The ratio values progressively increase from group *1a* (cpx Nd_n/Hf_n and Gd_n/Ti_n = 1.22 ± 0.50 and 1.98 ± 0.73), to groups *1b, 2b* and *2a* (Fig. 8b). The highest Gd_n/Ti_n and Nd_n/Hf_n values do not occur in wehrlites but in the *2a* cpx-poor lherzolites GG69 and GG73, followed by lherzolites GG104 and GG36. The correlation of these parameters suggests that the Hf and Ti relative depletion depends on the same cause. Zr, not shown, would provide evidence similar to Hf.

Ba, Th and U -The concentrations of these elements are extremely variable even within the same group. U always exhibits a positive spike in bulk-rock (caused by the high U concentration in carbonate drops into the secondary glass pockets, Laurora et al. 2001), it is always enriched with respect to Th in amphibole and varies from enriched to depleted in clinopyroxene.

Nb and Ta -Amphibole (and the rare phlogopite, Laurora et al. 2001) is the major host for these elements. The highest Nb concentrations occur in the Ti-poorest amphiboles. Most clinopyroxenes (Fig. 8c) and orthopyroxenes (not shown) have Nb/Ta values lower than PM (17.6), while amphiboles record higher values. The relatively high Nb/Ta ratios shown by amphiboles are consistent with their Mg# and Ti content, which, as shown by Tiepolo et al. (2001), should determine $^{Amph/L}D_{Nb/Ta} > 1$. When modally present, amphibole controls the Nb/Ta value of bulk rock.

Amphibole—clinopyroxene element distribution -$^{Amph/Cpx}D_{REE}$ is close to unity (Fig. 7d). Amphibole preferentially fractionates Nb, Ta, Ti, Sr and Ba.

Comparison with xenoliths affected by carbonatite metasomatism -Compared with the clinopyroxenes of the South-Eastern Australia xenoliths, typically affected by carbonatite metasomatism (Yaxley and Kamenetsky 1999), the group *1b, 2a* and *2b* clinopyroxenes have higher TiO_2 and Al_2O_3, lower Mg# and similar Na_2O concentration range. They also show weaker Ti depletion (Gd_n/Ti_n = 2.7–35.2 and 10.2–87.6, in our

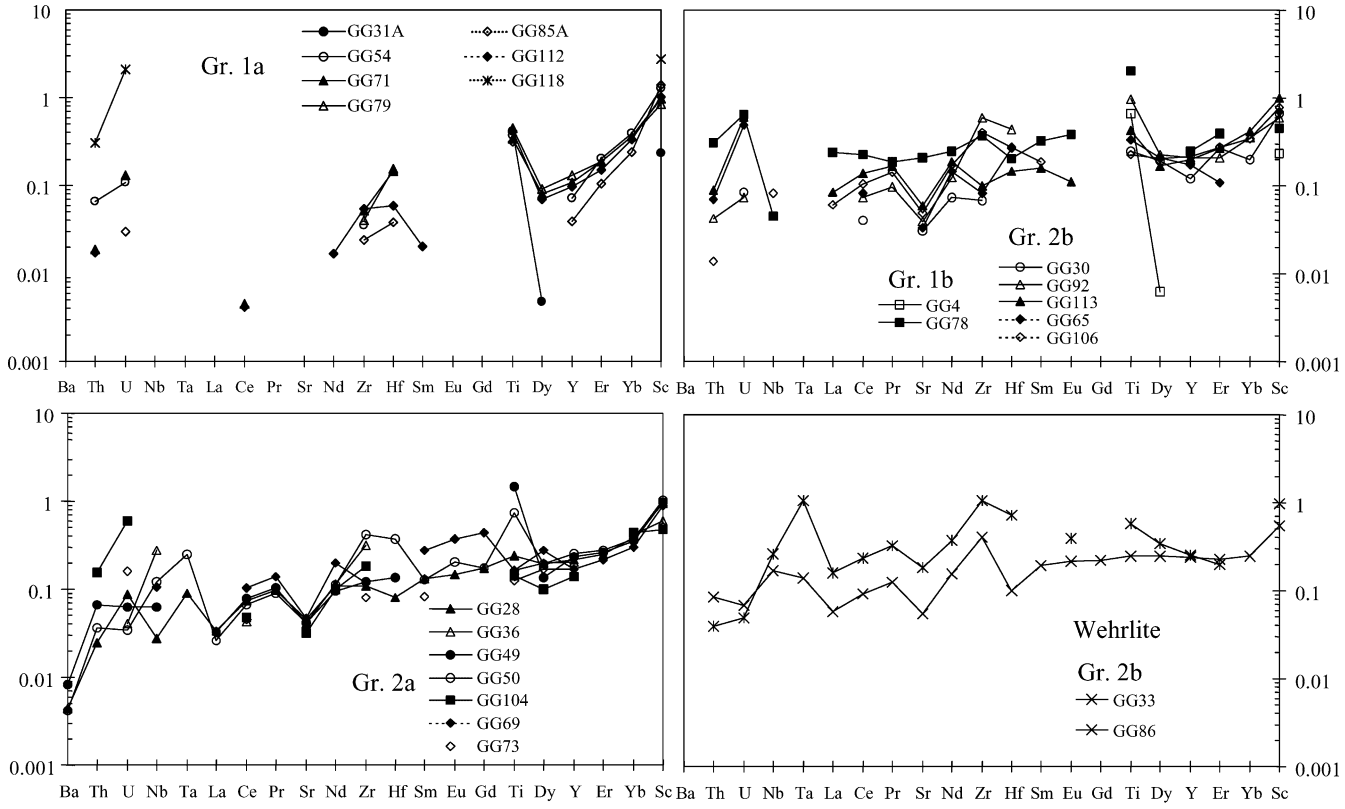

Fig. 6 Primitive mantle (Hofmann 1988)-normalised trace element profiles of orthopyroxene in the four xenolith groups and the two HTi wehrlites

samples and in the Australian xenoliths, respectively, Figs. 8b and 9a) and more marked Zr and Hf depletions ($Nd_n/Zr_n = 1.1–16.7$ and 1.1–5.3 and $Nd_n/Hf_n = 2.7–65.8$ and 0.9–24.1, respectively, Figs. 8b and 9c). The Southeastern Australia clinopyroxenes have a narrower Zr/Hf and Nb/Ta variation range (Fig. 8a and c). The Ti/Eu values are higher in the present cpx than in those of Southeastern Australia (129–1817 and 45–472, respectively) and only the *2b* clinopyroxenes partially overlap the Yaxley and Kamenetsky (1999) range.

Temperature and pressure

The average equilibrium temperatures (Table 2) calculated according to Brey and Köhler (1990) at 1.6 GPa are 905 ± 94, 1112 ± 22, 1087 ± 25 and 1084 ± 30°C in groups *1a, 1b, 2a* and *2b*, respectively. By using the Ca-in-olivine geobarometer of Köhler and Brey (1990), most xenoliths record a pressure range between 1 and 2.5 GPa, similar in the various groups, with outsider towards higher and lower values (Table 2). Higher temperature in amphibole-bearing than in coexisting anhydrous xenoliths, concomitant with different texture, is a common feature usually interpreted as a record of separate events (e.g. Stosch and Seck 1980). The group *1a* xenoliths could represent, therefore, the mantle untouched by the thermal-metasomatic event recorded in the other groups. In view of the similar texture, however, it is also possible that the observed thermal differences depend on the calibration of the geothermometers on anhydrous systems. Amphibole may influence the Fe, Mg and Ca distribution between cpx and opx.

Inconsistencies with carbonatitic metasomatism

Geochemical signatures commonly considered typical and indicative of carbonatite metasomatism are absent only in the group *1a* xenoliths, apart for their high CaO/Al_2O_3 and Na_2O/Al_2O_3 values, which may be anyway a consequence of the pervasive presence of glass-carbonate veins (Laurora et al. 2001; Rivalenti et al. 2004). Rivalenti et al. (2004) interpreted this group of xenoliths as representing the residuals of partial melting triggered by the addition of small-volumes of asthenospheric melts recording a slab signature in their H_2O and Cl abundance. The melting models reported in Figs. 4 and 5 show that the distribution and concentration of moderately incompatible elements (e.g. HREE) of bulk rock and clinopyroxene may correspond with 5–20% fractional melting residues. Differently, the relatively large concentration of highly incompatible elements may record the continuous mixing of the incremental melts with the uprising melt. In principle, this process can also account for the relatively large CaO/Al_2O_3 and Na_2O/Al_2O_3 of bulk rock. The whole-rock and pyroxene compositions of all the other groups variably display features believed to be consistent with carbonatite metasomatism. The previous description of modal and

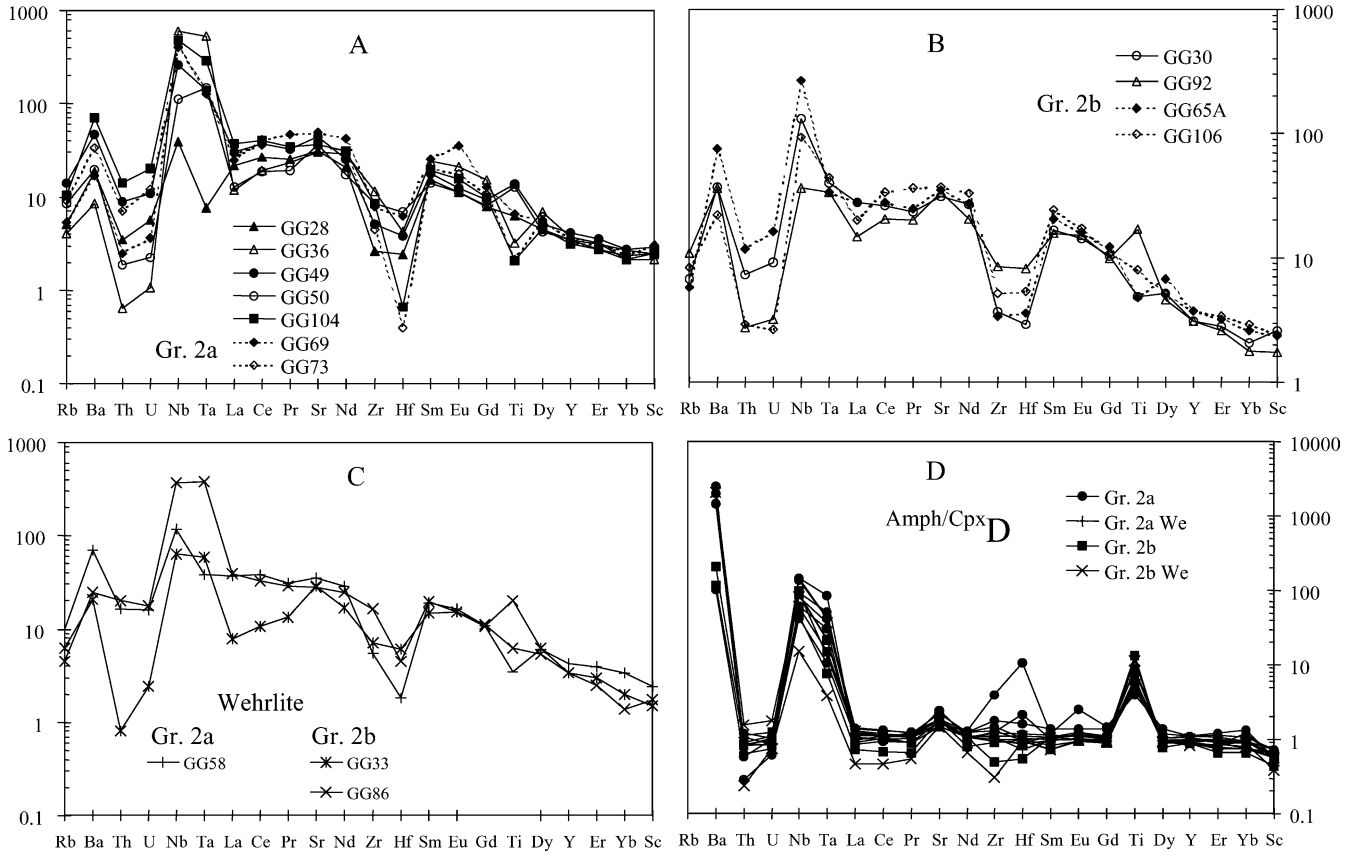

Fig. 7 a-c Primitive mantle (Hofmann 1988)-normalised trace element profiles of amphibole. **d** Amphibole/clinopyroxene trace element partitioning

geochemical variations highlights, however, important inconsistencies with the expected results of carbonatite metasomatism. These inconsistencies are:

1. Carbonatitic features appear also in the HTi xenoliths, recording geochemical features (high Ti, low Mg#) consistent with metasomatism operated by a basaltic component (Menzies et al. 1987);
2. Wehrlites, a potential end-product of carbonatitic metasomatism, do not display the most marked carbonatite fingerprints (e.g. the highest HFSE depletions and lowest Ti/Eu) and have relatively low Mg#. Moreover, two wehrlites follow the HTi variation trend;
3. Modal trends towards wehrlite occur in the HTi group, whereas instead the LTi *2a* group, having otherwise enhanced carbonatite characteristics, modally trends towards harzburgite;
4. Compared to those from xenoliths affected by carbonatite metasomatism, the GG clinopyroxenes display significant geochemical differences for both major (higher Al_2O_3 and TiO_2, and lower Mg#) and trace element (lower Ti, higher Zr and Hf depletions).

Moreover, doubts on carbonatite metasomatism rise from twin elements. Foley et al. (2001) have experimentally shown that clinopyroxenes in equilibrium with natrocarbonatite melts have Th/U < 1, while those in equilibrium with potassic alkaline melts (leucitite) have Th/U > 1. Here, most pyroxenes and amphiboles have Th/U higher than PM (Th/U = 4). In the sample group having the most marked Zr and Hf depletions (i.e. the most pronounced carbonatite characteristics, GG73, GG104, GG36 and GG69), the lowest Th/U is 1.97 (GG73). If the results of Foley et al. (2001) can be applied to mantle metasomatism involving sodic alkaline melts (which is unwarranted), the Th/U values of the GG phases suggest equilibration with silicate melts rather than carbonatite.

According to Green (1995) and Rudnick et al. (1993), large Zr/Hf and Nb/Ta values are indicators of carbonatite metasomatism. Figure 8d shows that in the GG clinopyroxene and amphibole Zr/Hf and Nb/Ta are decoupled, with the highest Nb/Ta displayed by samples having Zr/Hf ~40 (with one exception).

Two distinct metasomatic agents?

A possible way to reconcile the various petrological, mineralogical and geochemical indicators, which alternatively support basaltic and carbonatitic melt metasomatism, is to assume that these two agents acted independently and overprinted each other. This is a frequent explanation for localities with apparently contrasting metasomatic stiles, including GG (Gorring

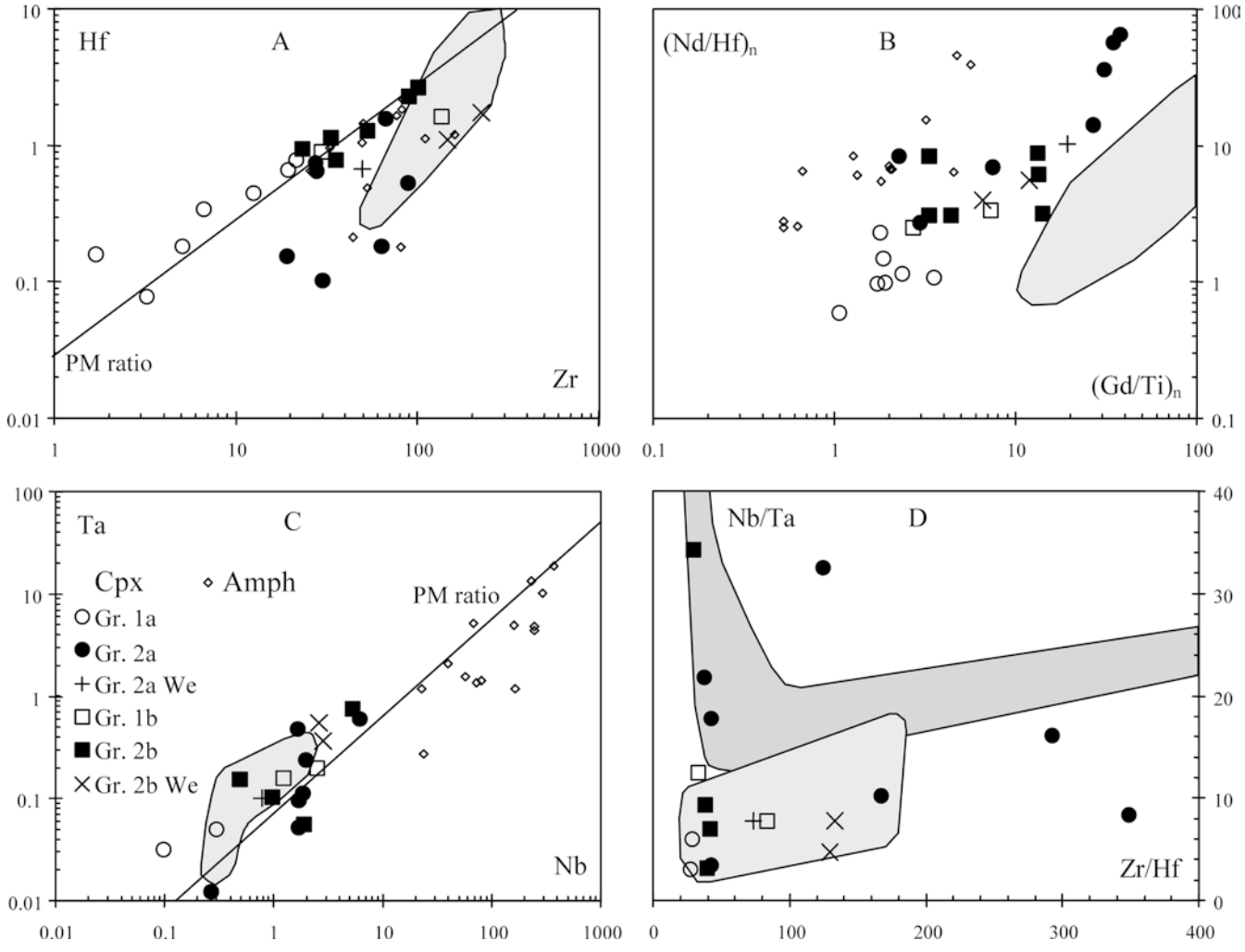

Fig. 8a–d Relationships of selected elements (ppm) and element ratios in clinopyroxenes and amphiboles. **a** Zr-Hf correlation, **b** Gd_n/Ti_n–Nd_n/Hf_n relationship, **c** Nb-Ta (ppm) correlation, **d** variation of Nb/Ta vs. Zr/Hf. Composition of the Australian clinopyroxenes (Yaxley and Kamenetsky 1999) is reported as a *light-shaded* field. Amphiboles in **d** are represented by the *dark-shaded* field

and Kay 2000). An alternative possibility is the infiltration of only one metasomatic agent (silicate melt) and geochemical variations induced by the reactions with the ambient peridotite during the porous flow of this agent. A simple test of these two hypotheses is provided by the variation trends of the geochemical parameters. In the first case, bulk rock and phase geochemistry would be a function of three components: pre-existing mantle, silicate melt and carbonatite component. As a consequence, the geochemical parameters of the metasomatised peridotites would randomly plot in the space defined by the three end-members. In the second case, geochemical variations should have as an end-member the pre-existing mantle composition and would be controlled by the reactive porous flow of the metasomatic agent and consequent geochemical variations. Since *natura non facit saltus* (Leibniz 1704), the geochemical variations should be steady and peaks should occur only in concomitance with dramatic events in the system, such as, for example, entering the stability field of a new phase, e.g. amphibole. Using these constraints, we examine the reciprocal behaviour of geochemical parameters expect to be different in carbonatitic and basaltic systems.

Element ratios vs. companion elements -The diagrams in Fig. 9 illustrate the influence of the companion element variations on the variation of Gd_n/Ti_n and Nd_n/Hf_n in clinopyroxenes and amphiboles. In the clinopyroxenes of the hydrous HTi and LTi xenoliths, the increase of the Ti and Hf concentrations correlate with a decrease of the negative HFSE anomaly. Zr (not shown) provides trends like Hf. The group *1a* and *1b* clinopyroxenes show the opposite behaviour. The two resulting variation trends meet at high HFSE concentration. The REE concentration also increases up to the HFSE cusp, but its increase at higher ratio values than that of the cusp is very modest. The cusp corresponds with the entry of amphibole in the peridotite assemblage.

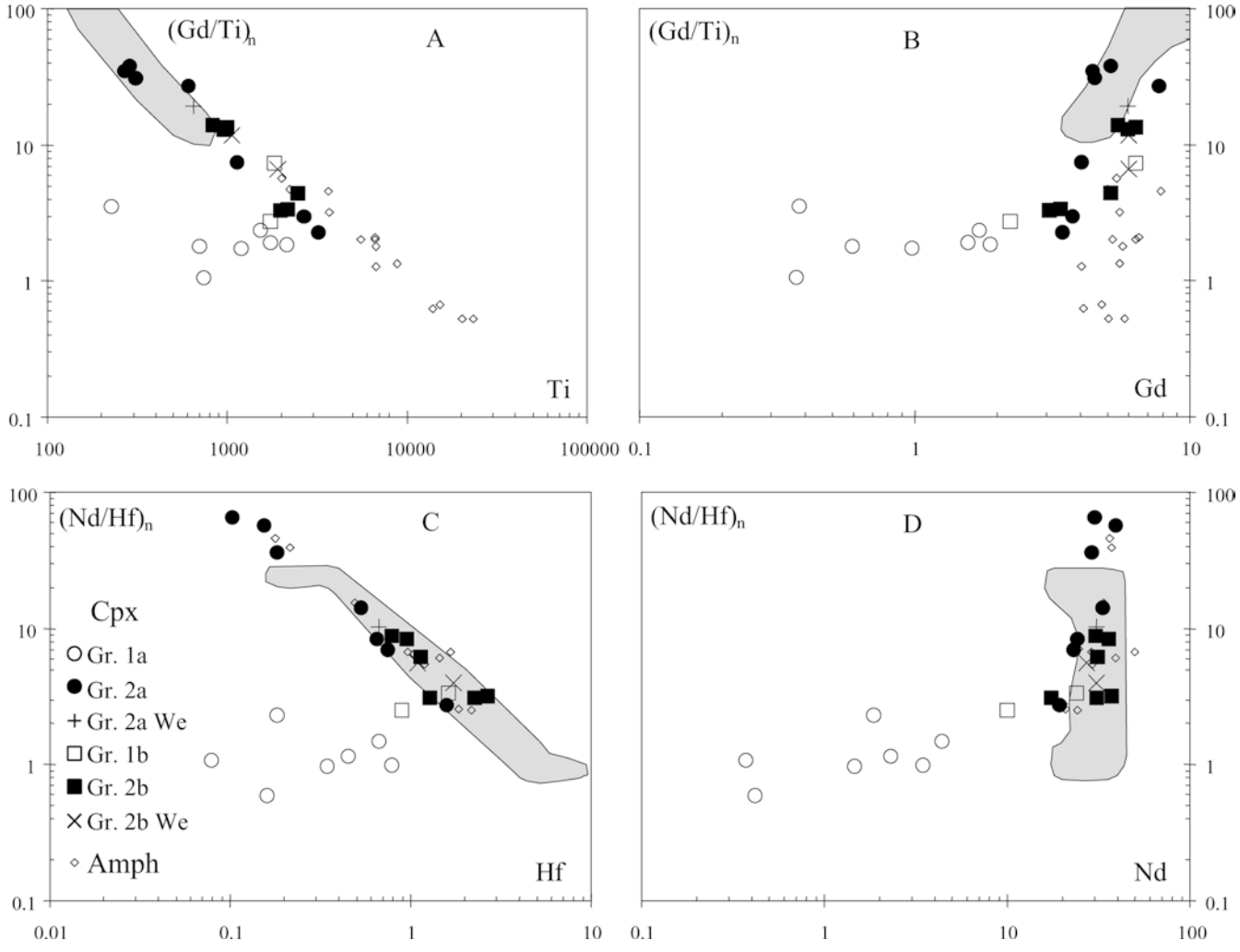

Fig. 9 Dependence of the HFSE anomalies (normalised to the primitive mantle, Hofmann 1988) from REE and HFSE concentrations (ppm) in the clinopyroxenes and amphiboles. The *shaded field* refers to the Yaxley and Kamenetsky (1999) clinopyroxenes reported for comparison

These variation trends are inconsistent with metasomatism of two potential end-members (alkali basalt, high HFSE and REE concentration, Nd_n/Hf_n and $Gd_n/Ti_n \sim 1$; carbonatite, low HFSE and high REE concentration, Nd_n/Hf_n and $Gd_n/Ti_n >> 1$) independently affecting a depleted mantle (low HFSE and REE concentration, Nd_n/Hf_n and $Gd_n/Ti_n \sim 1$) because of the lack of samples plotting in the gap between the depleted mantle component (*1a* samples) and the carbonatitic end-member. Rather, the trend suggests interaction with mantle of only one component, inducing metasomatic effects that drastically change during percolation. By applying the lever rule, the position and trend of amphibole in Fig. 9a suggests that the entry of amphibole in the reaction products may control the negative Ti anomaly of the percolating melt and, hence, of cpx.

Relationship Na_2O–HFSE anomalies -The diagrams of Fig. 10 illustrate the correlation between the Na_2O concentration of cpx (that should increase during carbonatite metasomatism) and the Ti and Hf anomalies. The resulting peculiar variation trend still presents a cusp at high Na_2O connecting two arrays of decreasing (array 1) and increasing (array 2) negative HFSE anomaly, respectively, with decreasing Na_2O. The sample distribution on the two arrays is, however, a little bit changed with respect to that shown in Fig. 9. Array 1 comprises the group *1a* and *1b* samples. Array 2 is constituted dominantly by the *2a* clinopyroxenes. The group *2b* clinopyroxenes plot on the two arrays close to the cusp. The lowest Mg# values occur in clinopyroxenes plotting close to the cusp. Amphibole mimics the cpx trend at higher Na_2O concentrations. The variation trend along array 2 is the contrary of what is predicted in carbonatite metasomatism. Note that the Yaxley and Kamenetsky (1999) clinopyroxenes behave like predicted by carbonatite metasomatism affecting a previous mantle of variable composition. Mixing of three components is unsupported at GG for the same reasons previously discussed (see anomalies-companion elements).

Relationship Na_2O/Al_2O_3–HFSE anomalies -The experiments of Blundy and Dalton (2000) indicate that

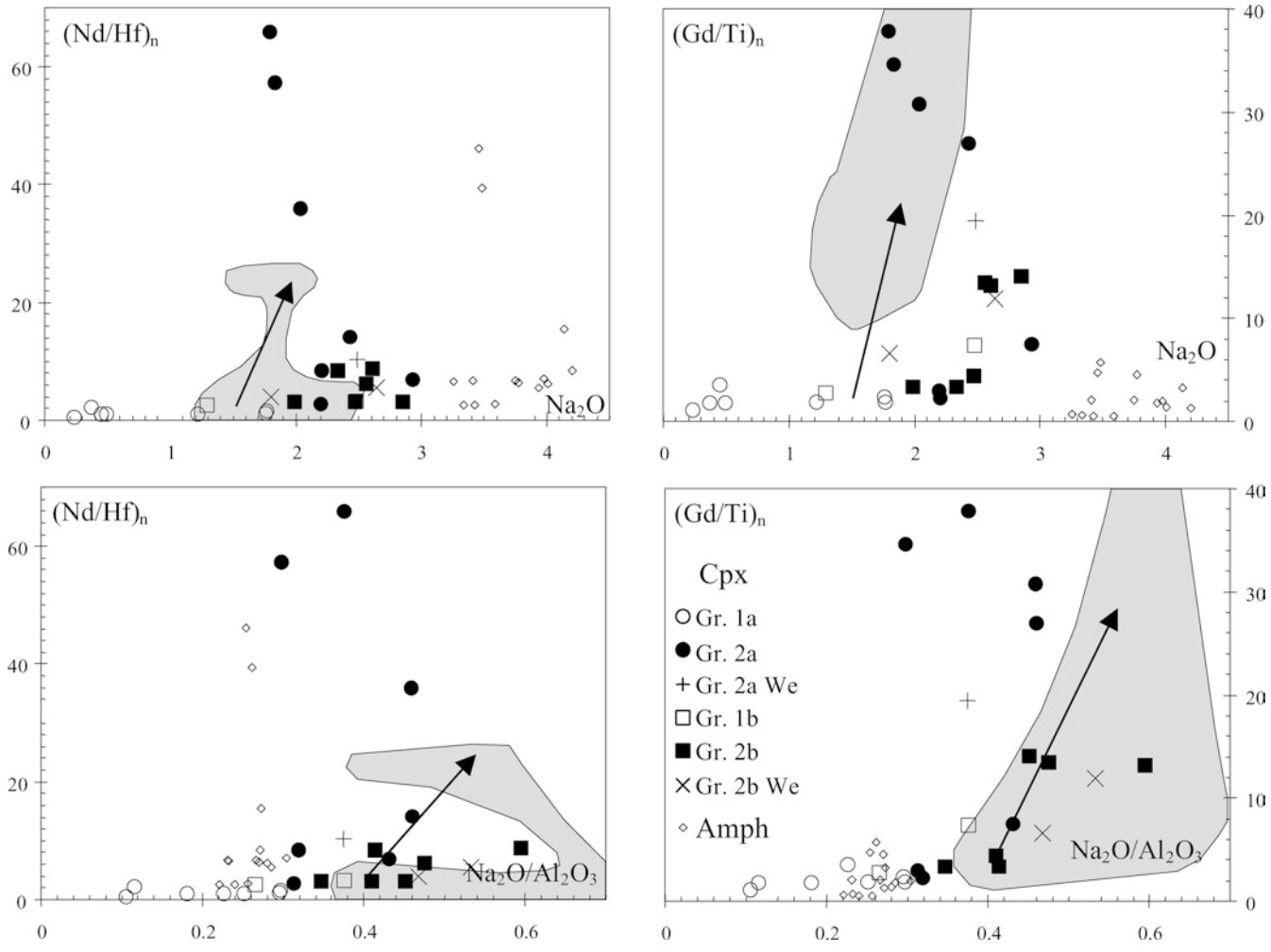

Fig. 10 Dependence of the HFSE anomalies (normalised to the primitive mantle, Hofmann 1988) from the Na_2O concentration (wt%) and the Na_2O/Al_2O_3 ratio in the clinopyroxenes and amphiboles. The *shaded field* refers to the Yaxley and Kamenetsky (1999) clinopyroxenes reported for comparison. The *arrows* indicate the variation trends qualitatively expected from carbonatitic metasomatism

carbonatite metasomatism should increase the Na_2O concentration with respect to that of Al_2O_3 in cpx. Our LTi group *2a* clinopyroxenes show an inverse correlation of the Na_2O/Al_2O_3 parameter with the HFSE anomalies (Fig. 10), contrasting with the positive correlation in the clinopyroxenes of Yaxley and Kamenetsky (1999).

Nature of the metasomatic agent

None of the points so far discussed supports carbonatite metasomatism overprinting a, or followed by, previous Fe-Ti metasomatism. The smooth variation trends in Figs. 8b, 9 and 10 favour metasomatism operated by only one agent, that percolated into, and reacted with, the ambient peridotite acquiring the observed geochemical features. The initial melt had to be an alkali basalt (because of the trend towards wehrlite of the HTi xenoliths, their high TiO_2/Al_2O_3 and relatively low Mg#). Various authors have proposed that silicate melts consumed during reactive porous flow into the ambient peridotite may leave a carbonatitic residual melt (Baker et al. 1998; Zanetti et al. 1999; Bodinier et al. 2004). This residual melt would induce a carbonatitic imprint in the peridotite. At Finero, for example, a mantle harzburgite was pervasively affected by silicate melt metasomatism that left a carbonatic residual fluid, documented in small peridotite pockets containing apatite and high-Na, HFSE depleted, cpx and modally trending towards wehrlite (Zanetti et al. 1999). By contrast, at GG, it has been shown that the clinopyroxenes having the highest relative HFSE depletions have the lowest Na (Fig. 10) and the modal trend is towards harzburgite. This suggests that the residual melt had to become silica-saturated, concomitantly with an apparently paradoxical increasing HFSE depletion (trend towards harzburgite of the LTi xenoliths concomitant with their high HFSE negative anomalies). Variation of initially alkaline melts to silica-rich melts is a typical result of melt-peridotite reaction at lithospheric levels (Kelemen et al. 1992, 1998; Shaw 1999), because the mineralogical reaction is

ubiquitously dominated by dissolution of peridotite orthopyroxene.

The alternative possibility on the nature of the metasomatic agent, hydrous fluid rather than melt, was discussed by Laurora et al. (2001). Moine et al. (2001) also proposed that the variable REE/HFSE values shown by amphiboles from peridotite xenoliths from Kerguelen Island (Indian Ocean) could be the result of changes of the mineral/liquid trace elements partitioning as a function of aH_2O. The ability of fluids in inducing HFSE-REE decoupling is commonly based on the results of the experimental work at low pressure done by Keppler (1996). Nevertheless, successive experimental works on fluid/melt (Ayers and Eggler 1995; Adam et al. 1997) and fluid/solid partitioning (e.g. Stalder et al. 1998) at high P and T did not confirm the occurrence of significant HFSE fractionation between melt and fluid. Therefore, the conclusion that large REE/HFSE fractionation can be a marker of fluid percolation is, at least, disputable.

Constraints on the metasomatic process

HFSE-REE decoupling is frequently documented in hydrous mineral-bearing peridotites, and indirectly supported by the occurrence of positive Hf and, less frequently, Zr anomaly in clinopyroxenes and amphiboles from mantle peridotites and cumulates (e.g. Grégoire et al. 2000a; Ionov et al. 2002; Raffone et al. 2004) and amphibole-rich veins in peridotite (Moine et al. 2001). Neglecting carbonatite metasomatism, this decoupling may originate either from the dissolution-crystallisation of phases having $^{S/L}D_{HFSE}{}^{4+}$ higher than those of the adjacent REE or be inherited from processes related with the source of the metasomatic agent or its percolation in the mantle region beneath that of observation (e.g. hidden garnet facies and observed spinel facies).

Structural-compositional variation of the metasomatic phases during porous flow may induce important variations of the partition coefficients. For example, Hill et al. (2000) demonstrated that, when clinopyroxene becomes enriched in $^{[4]}$Al component, $^{Cpx/L}D_{HFSE}{}^{4+}$ become > 1 and > $^{Cpx/L}D_{adjacent\ REE}$. At GG, however, the variation range of $^{[4]}$Al is much narrower than that of the Hill et al. (2000) experiments. Tiepolo et al. (2000, 2001) and Oberti et al. (2000) show that, as a response to compositional and structural variations of amphibole, compatibility of Ti substantially increases, whereas Nb and Hf become compatible in amphiboles in equilibrium with Ti-depleted, silica-rich melts. The $^{Amph/L}D_{Zr,Ta}$ also increase, but they can more hardly become compatible, being the $^{Amph/L}D_{Nb/Ta}$ and $^{Amph/L}D_{Hf/Zr}$ about 1.5-2 in alkaline systems differentiated via Ol + Cpx + Amph ± Phl crystallisation (namely, SiO_2 - and FeO-rich and TiO_2 -poor). Amphibole crystallisation would further deplete the percolating melts in Ti and, as shown in Fig. 8d, in clinopyroxenes in equilibrium with these melts high Zr/Hf would correspond with relatively low Nb/Ta. None of the experimental works quoted above reports, however, substantial HFSE-REE decoupling and do not explain, therefore, the observed $HFSE^{4+}$ negative anomalies. Consistently, Ionov et al. (2002), who used $^{S/L}D$ pertinent to SiO_2 -undersaturated high-P-T systems for modelling metasomatism documented in Spitsbergen xenoliths, show that crystallisation of amphibole during melt/spinel peridotite reaction can determine negative Nb, Ta and Ti anomalies in the differentiates, but not negative Zr and Hf anomaly.

Orthopyroxene and phlogopite preferentially host Zr, Hf and Ti with respect to REE (Salters et al. 2002; McDade et al. 2003) and could in principle induce REE-HFSE decoupling in the flowing melt. However, their $^{S/L}D_{Zr,Hf}$ are so low that hardly their crystallisation could cause relevant anomalies.

Metasomatic oxides able to selectively fractionate HFSE has been used to explain the anomalies of these elements (e.g. Bodinier et al. 1996, 2004; Bedini et al. 1997). Titanium oxides, such as ilmenite, armalcolites and the minerals of the crichtonite series have been recently recognised to be quite diffuse (Grégoire et al. 2000b; Kalfoun et al. 2002). Bodinier et al. (1996) documented the occurrence of titanium oxides such as Nb-rutile on the surface of peridotite spinel. Ulvospinel can also be present in alkaline cumulate xenoliths (e.g. Raffone et al. 2004). At GG, Ti oxides have not been found in connection with the metasomatic amphiboles and pyroxenes, but only in melt pockets related to the infiltration of the host basalt, as well as to decompression melting of hydrous minerals (Laurora et al. 2001). If, anyway, they were there during the metasomatic event, they may not have been rutile and ilmenite, which have very high $D_{Nb(Ta)}$ values (in the range 100–500; Green and Pearson 1987; Stimac and Hickmott 1994 and references therein; Jenner et al. 1993; Foley et al. 2000) and $D_{Nb(Ta)}$ /$D_{Zr(Hf)}$ ratio, and would thus produce results in contrast with the large Nb(Ta) absolute concentration and Nb/Zr ratios shown by the GG clinopyroxenes. Notwithstanding the absence of experimental $^{S/L}D$, armalcolites and minerals of the chrichtonite series (including loveringite) are more suitable because they can have $D_{Zr(Hf)}$ > to > > $D_{Nb(Ta)}$. In particular, if the mean of the concentration reported by Kalfoun et al. (2002) and Grégoire et al. (2000b) is compared with that of a common OIB, the $D_{Nb(Ta)}$ result in the range 1–10, whereas $D_{Zr(Hf)}$ are in the range of 10–100 for chrichtonite series minerals.

The parameters so far examined are implicitly assumed to have operated during the reactive porous flow of the metasomatic agent in to the observed spinel-facies mantle. It is, however, also possible that the melt infiltrating the GG spinel-facies mantle had previous, weak HFSE depletion either inherited from the melt source or acquired during percolation in the garnet-facies segment. The possibility that the melt infiltrating the spinel-facies GG mantle had initial, weak HFSE depletions, concomitant with the alkaline character of the melt, is consistent with the model of Rivalenti et al. (2004). They

proposed that slab-derived components fertilised asthenospheric domains of the mantle wedge, from which small volume melts migrated and interacted with the spinel-facies lithosphere. Near-solidus melts derived from such fertilised asthenosphere would be ne-normative (Yaxley and Green 1998). Although the experiments of Rapp et al. (1999) do not show relative HFSE depletion in eclogite-derived melts, but rather enrichment, van Westrenen et al. (2001) emphasise that Zr, Hf and Ti depletions could occur in silicate melts derived from eclogites because these elements are compatible, and adjacent REE incompatible, in Ca-rich garnet. The other possibility, relative HFSE depletion in the melt during percolation in the garnet-facies mantle, is supported by experimental results showing that $^{Gnt/L}D$ for Zr and Hf can be greater than those of all LREE in the P range 3.4-2.5 GPa (Hauri et al. 1994; van Westrenen et al. 2001; Salters et al. 2002). Garnets from the Vitim peridotite xenoliths have both Zr_n and Hf_n enriched with respect to Sm_n (Ionov 2004; see also, for similar results, Xu et al. 2000, and, only for Hf, Qi et al. 1995). Consistent variation of the Zr(Hf)/Sm fractionation has been also documented for the garnet/fluid equilibrium (Stalder et al. 1998). The possible role of garnet could also partially explain the large variability of the Zr/Hf ratio, because such elements can enter both X and Y sites of the garnet structure, D_{Zr}/D_{Hf} thus varying from >1 to <1 (van Westrenen et al. 2001).

Theoretical modelling

In the previous sections, it has been discussed how the changes in bulk-rock and mineral compositions of groups *1b, 2a* and *2b* can be rationalised in terms of transient effects related to differentiation of one component (alkaline melt) via reactive porous flow. In order to support that at GG such a process may be a viable alternative to carbonatite metasomatism, we present the results of two reactive porous flow models, made according to the Vernières et al. (1997) procedure. The first model will focus on the explanation of the geochemical dilemma represented by the clinopyroxene and bulk-rock trace element composition of groups *1b, 2a* and *2b* GG xenoliths, which have virtually the same REE concentration but dramatically different REE/$HFSE^{4+}$ fractionation (e.g. see the clinopyroxene composition of GG92 and GG73 samples). The second model will focus on the possible effects of the porous flow migration through garnet-facies peridotites on the REE/HFSE and LREE/HREE fractionation of the uprising melts.

Model 1

The geochemical and petrographic features of GG xenoliths allow us to set the following preliminary constraints on the modelling:

The composition of the lithospheric spinel peridotite protolith -Numerical simulations reported in the literature have shown that reactive melt migration in the lithospheric mantle is particularly efficient in inducing large geochemical variations when the ambient peridotite is depleted (lherzolite to strongly refractory harzburgite, e.g. Bedini et al. 1997; Ionov et al. 2002). Rivalenti et al. (2004) have shown that the only Patagonia xenoliths where metasomatism did not hide the evidence of previous composition and processes were rare harzburgites having porphyroclastic texture and representing residues of variable, but large, partial melting (~20% fractional melting). These peridotites are modally (depletion of clinopyroxene, absence of hydrous minerals) and geochemically (large depletion in moderately incompatible elements, e.g. HREE, Ti) similar to the group 1a GG xenoliths, from which they differ for texture, that is invariably secondary and deeply re-crystallised in the latter (Gorring and Kay 2000; Laurora et al. 2001; this work). The group *1a* xenoliths, can be considered, therefore, as a model for the composition of the mantle predating metasomatism. Thus, the composition of harzburgite GG118 has been adopted as representative of the ambient peridotite before injection of alkaline melts.

The partition coefficients and the trace element composition of the infiltrated melt -Most porous-flow literature models used partition coefficients determined for relatively high T and P (e.g. Ionov et al. 2002). In particular, the clinopyroxene-liquid partition coefficients most frequently used were those of Hart and Dunn (1993), which were obtained at 3 GPa and 1380°C in a SiO_2-undersaturated anhydrous system. This data set, or similar ones, were successfully applied in the simulation of partial melting processes for reproducing the observed REE composition of refractory clinopyroxenes (e.g. Johnson et al. 1990) and furnished very reasonable estimates for liquids in equilibrium with clinopyroxenes from cumulates (e.g. Koga et al. 2001) or reactive dunite and harzburgite (Kelemen et al. 1995). Nevertheless, it is a common observation that, when the Hart and Dunn's data set is applied in combination with the composition of clinopyroxenes from peridotite metasomatised by hydrous alkaline melts *s.l.*, the REE content and the LREE/HREE fractionation of the calculated liquid frequently exceed those found in natural silicate melts. For this reason, Ionov et al. (2002) concluded that geochemical features of bulk-rock and minerals similar to those of the GG group 2 xenoliths (their Type II samples) couldn't be explained by percolation of the host basalt with clear OIB affinity. Alternatively, they invoked the occurrence of an extremely fractionated and LREE-enriched silicate (carbonate) melt. On the other hand, a discrete number of papers have shown that the $^{Cpx/L}D_{REE}$ documented in clinopyroxene-glass pairs from mantle xenoliths can be significantly higher than those of Hart and Dunn, being $^{Cpx/L}D$ for HREE even higher than one (e.g. Chazot et al. 1996; Vannucci et al. 1998; Laurora et al. 2001). Similar D_{REE} values have been experimentally determined by

Blundy et al. (1998) for near-solidus melting of fertile spinel peridotite. The possibility to estimate solid-melt trace-element partitioning for near-solidus conditions in the GG xenoliths is provided by the occurrence of clinopyroxene-glass pairs. As documented by Laurora et al. (2001), the observed $^{Cpx/L}D_{REE}$ are significantly higher than those of Hart and Dunn (1993). Liquid compositions calculated by using this data set still show larger LREE content and LREE/HREE fractionation than the GG alkaline lavas reported by Gorring and Kay (2001), but approach the composition of Ti-rich glasses from GG xenoliths. This suggests that this data set may document the REE composition of the metasomatic melt. Thus, the trace element composition of the infiltrating liquid was estimated by using the $^{Cpx/L}D$'s measured in GG xenoliths (Table 6) and the composition of the clinopyroxene from the Fe-Ti-richer sample (GG92), assuming this latter as that closest to the chemical equilibrium with the more primitive alkaline melt. The $^{Cpx/L}D_{REE}$ from the GG xenoliths were also used in the numerical simulation. In addition, the solid-liquid trace-element partitioning for amphibole, orthopyroxene, olivine and oxide were calculated as reported in the caption of Table 6, in order to produce a consistent data set.

Mineralogical reactions and model results -Mineralogical reactions were designed to involve amphibole, clinopyroxene, olivine and HFSE-rich oxide crystallisation without assimilation of peridotite minerals. These assumptions determined a decreasing melt mass with the progression of the interaction. The mantle column was considered composed by 50 cells and 150 process increments were run. Melt crystallisation was set to 0 and 2% at the base and at the top of the column, respectively. After 150 process increments, the melt fraction (porosity) varies steadily from 3% (at the base of the mantle column) to 6‰ (50th cell), whereas the final composition varies from 74% Ol, 22.7% Opx, 3.3% Cpx (first cell) to 73% Ol, 22.3% Opx, 3.8% Cpx, <0.1% Ox, 0.9% Amph (50th cell).

Figure 11a shows the composition of liquid each 10 cells after 150 increments. Liquid composition reveals that the REE concentration of the entire mantle column approaches the equilibrium with the melt injected at its base. Differently, the crystallisation of very small amounts of HFSE-rich oxides is able to determine a "sink" effect for $HFSE^{4+}$ with consequent development of strong REE/HFSE fractionation. In particular, the strong REE/$HFSE^{4+}$ fractionation peculiar of the liquid calculated in equilibrium with the GG73 clinopyroxene is accurately matched by the liquid composition of the cells close to 40th. The weakness points of this model are the uncertainty about the oxide-melt

Table 6 Chemical and reaction parameters used in numerical modelling

	$^{Ol/L}D$[c]	$^{Opx/L}D$[b]	$^{Cpx/L}D$[a]	$^{Oxide/L}D$[d]	$^{Amph/L}D$[b]	Infiltrated melt[e] (ppm)
Chemical parameters						
Th	1.77E-07	2.12E-04	2.12E-02		2.00E-02	12.5
U	1.32E-07	2.64E-04	1.32E-02		2.00E-02	5.1
Nb	2.95E-04	4.66E-04	1.14E-02	3.20E+00	1.14E+00	42.9
Ta	7.50E-04	1.24E-03	3.75E-02	5.70E+00	5.20E-01	4.1
La	2.31E-04	2.62E-04	1.25E-01		1.50E-01	102
Ce	5.37E-04	8.31E-04	2.31E-01		2.60E-01	205
Sr	7.86E-05	2.11E-04	1.01E-01		1.70E-01	3314
Nd	1.08E-03	2.53E-03	5.05E-01		5.20E-01	61.2
Zr	1.20E-02	1.60E-02	3.90E-01	1.30E+02	4.50E-01	230
Hf	2.30E-02	4.36E-02	7.65E-01	1.60E+02	9.70E-01	3.0
Sm	1.15E-03	7.61E-03	7.61E-01		8.10E-01	10.9
Gd	1.85E-03	2.82E-02	9.72E-01		1.03E+00	5.3
Ti	1.69E-02	3.19E-01	7.96E-01	2.10E+01	4.03E+00	1702
Dy	3.56E-03	4.16E-02	1.13E+00		1.10E+00	3.4
Ho	4.44E-03	6.00E-02	1.06E+00		1.01E+00	0.65
Er	5.35E-03	8.30E-02	9.89E-01		8.60E-01	1.6
Yb	8.87E-03	1.47E-01	1.05E+00		1.05E+00	1.1

	Ol	Opx	Cpx	Oxide	Amph
Modal parameters					
Crystallised minerals[f]	0.20		0.30	0.05	0.45

[a] $^{Cpx/L}D$s: average $^{Cpx3/glass}D$s in xenoliths GG58, GG73 and GG104 (Laurora et al. 2001)

[b] $^{Opx/L}D$s and $^{Amph/L}D$s calculated from the $^{Cpx/L}D$ and the Opx/Cpx and Amph/Cpx values in the GG samples

[c] $^{Ol/L}D$s: calculated from the $^{Cpx/L}D$ and the Ol/Cpx ratio desumed by the $^{Ol/L}D$ and $^{Cpx/L}D$ reported by Ionov et al. (2002) $^{Cpx/L}D$ and the Ol/Cpx ratio inferred from the $^{Ol/L}D$ and $^{Cpx/L}D$ reported by Ionov et al. (2002)

[d] $^{Oxide/L}D$s: calculated from the average chrictonite mineral compositions (Kalfoun et al. 2002) and OIB composition (Sun and McDonough 1989). $^{Oxide/L}D_{Hf}$ modified according to the experimental D_{Zr}/D_{Hf} ratio from rutile/titanate-melt equilibrium (Foley et al. 2000; Tiepolo et al. 2002)

[e] Infiltrated melt composition: calculated on the basis of the $^{Cpx/L}D$s and Cpx composition from the Fe-and Ti-richer sample (GG92)

[f] Deduced from the modal composition of the GG samples

Table 7 Chemical and modal parameters used in numerical simulation of melt/peridotite reaction at garnet-facies conditions

	$^{Ol/L}D$[a]	$^{Opx/L}D$[a]	$^{Cpx/L}D$[a]	$^{Gnt/L}D$[a]	Infiltrated melt[b] (ppm)	Initial peridotite[c] (ppm)
Chemical parameters						
Th	5.00E−05	2.70E−03	1.77E−02	1.30E−02	4.00	0.00048
U	4.70E−04	2.40E−03	2.16E−02	5.50E−02	1.02	0.00034
Nb	1.70E−04	4.00E−03	2.40E−02	1.60E−02	48	0.0053
La	6.00E−08	1.60E−03	2.60E−02	6.20E−04	37	0.00002
Ce	7.50E−07	3.10E−03	3.60E−02	3.20E−03	80	0.0033
Nd	1.20E−05	9.50E−03	6.20E−02	4.60E−02	38.5	0.024
Zr	4.45E−03	1.30E−02	3.80E−02	3.69E−01	280	0.80
Hf	3.74E−03	3.20E−02	8.40E−02	3.96E−01	7.80	0.037
Sm	1.20E−04	2.00E−02	9.00E−02	2.68E−01	10.0	0.032
Gd	6.00E−04	3.10E−02	1.15E−01	7.88E−01	7.62	0.10
Ti	1.09E−02	1.04E−01	1.30E−01	2.69E−01	17,200	237
Dy	3.70E−03	4.10E−02	1.38E−01	1.57E+00	5.60	0.21
Ho	7.20E−03	4.40E−02	1.47E−01	1.90E+00	1.06	0.054
Er	1.35E−02	4.60E−02	1.54E−01	2.11E+00	2.62	0.17
Yb	4.10E−03	4.60E−02	1.63E−01	5.15E+00	2.16	0.27

	Ol	Opx	Cpx	Gnt
Modal parameters				
The initial peridotite	0.657	0.281	0.009	0.053
Cristallised minerals	1			

[a]Solid–liquid partition coefficients: Salters et al. (2002). REE data sets: checked and completed by fitting the experimental data to the formulation of the elastic-site lattice-strain theory (Blundy and Wood 1994)

[b]OIB: Sun and McDonough (1989)

[c]Initial lithospheric peridotite: residue from 18% batch melting of garnet-facies PM source (Hofmann 1988)

partitioning and the lack of HFSE-oxides in the peridotite assemblages. On the other hand, at GG Ti-oxides are rather frequent in melt pocket and vein determined by decompression melting of amphibole and/or peridotite mineral/host basalt reaction. Thus, we conclude that HFSE-oxide can actually be an important mineral during the first stages of melt-peridotite reaction, playing a leading role in the generation of transient REE/HFSE fractionation.

Model 2

The second model (Fig. 11b) refers to percolation of an OIB-like melt (composition taken from Sun and McDonough 1989) into the hidden, garnet-facies mantle segment, and is aimed to show the effects on this process on the melt infiltrating the spinel-facies mantle in terms of REE/HFSE and LREE/MREE fractionation. Model parameters are reported in Table 7 and in the Fig. 11b caption. According to the depleted character previously inferred for the pristine Patagonia lithosphere, it was assumed that the mantle was constituted by a depleted garnet-harzburgite, whose modal and chemical composition (Table 7) was calculated by 18% batch melting (melting mode from Walter 1998) of Primitive Mantle (Hofmann 1988). It was assumed that the melt/peridotite mineralogical reaction involved no assimilation and the crystallisation of only olivine. Thus, percolation occurred at decreasing melt mass, as in Model 1. Solid/liquid partition coefficients for garnet-facies assemblages were taken from Salters et al. (2002), whose data set was completed on the basis of the numerical formulation of the lattice-site elastic-strain theory by Blundy and Wood (1994). A mantle column formed by 20 reaction cells was considered and, in order to highlight the fractionation produced by this interaction, the liquid compositions after only 20 increments are shown in Fig. 11b. Under these assumptions, during percolation the liquid composition was characterised by an increase of LREE, whereas the HREE content was rapidly buffered to low content, with a consequent increase of LREE/HREE fractionation. As for HFSE, liquids acquired variable Zr and Hf depletion with respect to L-MREE, whereas the REE/(Ti, Nb) ratio was virtually unaffected. Interestingly, REE, Th, U, Zr and Hf concentrations in liquids approached (close to 10th cell) that of the hypothetical liquid calculated in equilibrium with the cpx from GG92 sample.

This evidence suggests that the melt-garnet harzburgite reaction could be relevant in the production of transient features like large LREE/HREE and REE/(Zr, Hf) fractionation frequently documented in metasomatised spinel-peridotites from world-wide occurrences (e.g. Rivalenti et al. 2000; Ionov et al. 2002; Bodinier et al. 2004), revealing, moreover, a possible cognate origin with the alkaline melts commonly erupted to the Earth's surface.

Conclusions

The Gobernador Gregores xenoliths consist of: (1) anhydrous lherzolites and harzburgites recording

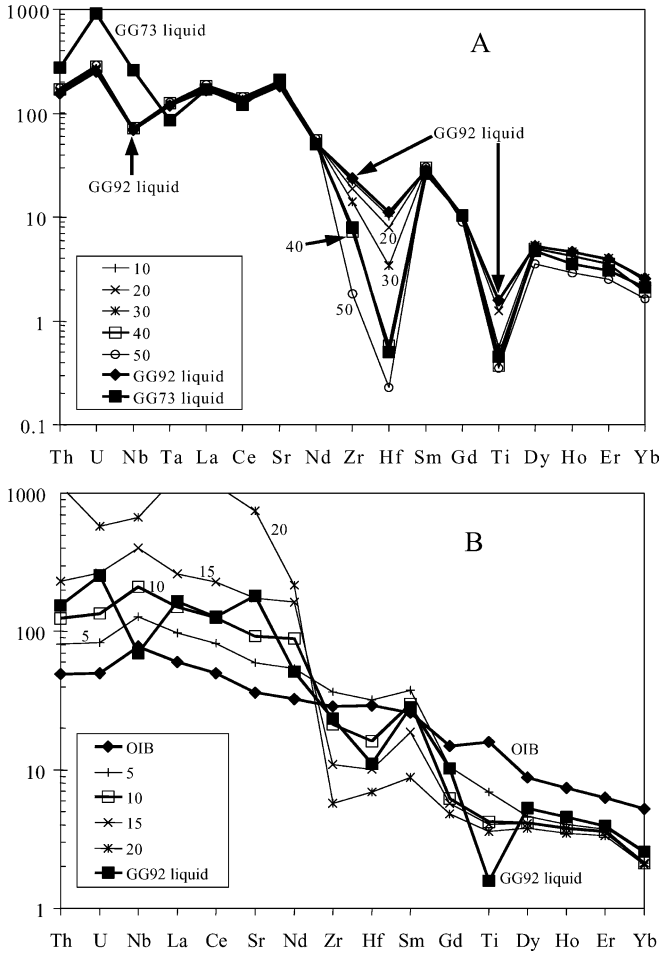

Fig. 11 **a** Trace elements compositions of liquids calculated by means of Plate Model simulation (Vernières et al. 1997) of the reaction between an alkaline melt and refractory spinel harzburgite. Initial and final liquid compositions: potential melt in equilibrium with the GG92 and GG73 cpx, respectively. Chemical composition of the ambient peridotite: spinel harzburgite GG118. Further chemical and modal parameters and details on the process are reported in Table 6 and in the text. The model is able to reproduce the $REE/HFSE^{4+}$ fractionation at nearly constant REE content shown by mineral chemistry of groups *2a* and *2b* samples. Conversely, the $HFSE^{5+}$, U and Th fractionation are poorly documented. **b** Trace elements compositions of liquids calculated by Plate Model simulation (Vernières et al. 1997) of the reaction between OIB and refractory garnet harzburgite. OIB composition: Sun and McDonough (1989); garnet harzburgite composition: 18% batch melting residue of a garnet-facies, PM source (Hofmann 1988). Further chemical and modal parameters and details on the process are reported in Table 7 and in the text. Liquid compositions are shown for the first cell (corresponding to the injected OIB) and for every 5 cells. They document that OIB-garnet peridotite interaction can produce a significant Zr and Hf depletion with respect to L/MREE, but not Ti and Nb depletion. The REE, Th, U, Zr and Hf concentrations approach that of the hypothetical liquid calculated in equilibrium with the Cpx from GG92 sample (see text and Table 7). Between 1 and 15 cells, the final porosity varies from 3% to 6‰, whereas the final composition is constantly 66.4% Ol, 27.5% Opx, 0.9% Cpx, 5.2% Gnt

melt–assisted partial melting (group *1a*); (2) anhydrous and hydrous xenoliths modally trending towards wehrlite, having high TiO_2/Al_2O_3 ratios both in bulk-rock and mineral phases, and REE profiles similar to those induced by alkali basalt metasomatism (groups *1b* and *2b*, respectively); (3) hydrous xenoliths modally trending towards harzburgite, having low TiO_2/Al_2O_3 (group *2a*) and REE patterns similar to groups *1b* and *2b*. The Ti, Hf and Zr negative anomalies progressively increase in the order *1a, 1b, 2b* and *2a*, the most marked occurring in *2a* cpx-poor lherzolites. The Na_2O, Ti, Hf and Zr concentrations increase in correlation with the negative HFSE anomalies only in the pyroxenes and amphiboles of the anhydrous xenoliths, but instead they decrease in the hydrous ones, while REE concentration remains roughly constant and high.

Most of the modal and geochemical features are, therefore, inconsistent with carbonatitic metasomatism, that would induce modal trends towards wehrlite, increase of the Na_2O and REE concentration and negative HFSE anomalies in silicate phases of xenoliths that experienced large carbonatite interaction. For the same reason they are also inconsistent with processes where a carbonatite residual melt derives from consumption of an initially silicate melt during reactive porous flow. Rather, the observed characteristics are consistent with reactive porous flow of an initially ne-normative, hydrous basalt inducing the characteristics of the *2b* xenoliths, that evolves to silica saturation (e.g. the *2a* xenoliths). Amphibole crystallisation and the variations of the $^{Amph/L}D_{HFSE}$ caused by changes in the composition of the flowing melt may explain the depletion of Ti with respect to REE, the variations in clinopyroxenes and amphiboles of the Nb/Ta ratio from higher to lower than chondritic and of the Zr/Hf ratio from chondritic to higher than chondritic. No experimental work yet available indicates, however, any important REE-Zr, Hf decoupling in amphibole and crystallisation of this phase cannot, therefore, explain the Zr and Hf depletions observed in the group *2a* xenoliths. All the observed geochemical features may be explained by hypothesising the presence of a mineral of the crichtonite series in the metasomatic assemblage and we present a numerical modelling (Plate Model, Vernières et al. 1997) where the observed characteristic are successfully reproduced by the crystallisation of olivine, clinopyroxene, amphibole and loveringite in the flowing melt. Numerical modelling also shows that modest HFSE anomalies may be present in the initial melt infiltrating the spinel-facies as a heritance of reactive porous flow into the garnet-facies mantle. The latter process also is particularly effective in determining a significant increase of the LREE/HREE fractionation in the migrating liquids, thus potentially explaining the very large LREE-enrichment frequently documented in mineral and bulk-rock chemistry of peridotite metasomatised by asthenospheric alkaline melts.

Acknowledgements We thank the FOMICRUZ agency and R. Barrenechea for the facilities and help they provided during the field work in Patagonia. Jean-Louis Bodinier is greatly thanked for having kindly provided the Plate Model software. We gratefully acknowledge the constructive revisions by M. Grégoire and M. Menzies. This research was financially supported by MURST

(COFIN 1998 and 2000), CRN and CNR-CONICET joint programmes.

References

Adam J, Green TH (2001) Experimentally determined partition coefficients for minor and trace elements in peridotite minerals and carbonatitic melts, and their relevance to natural carbonatites. Eur J Mineral 13:815–827

Adam J, Green TH, Sie S, Ryan CG (1997) Trace element partitioning between aqueous fluids, silicate melts and minerals. Eur J Mineral 9:569–584

Ayers JC, Eggler DH (1995) Partitioning of elements between silicate melt and H_2O–NaCl fluids at 1.5 and 2.0 GPa pressure: Implications for mantle metasomatism. Geochim Cosmochim Acta 59:4237–4246

Baker MB, Stolper EM (1994) Determining the composition of high-pressure mantle melts using diamond aggregates. Geochim Cosmochim Acta 58:2811–2827

Baker J, Chazot G, Menzies M, Thirlwall M (1998) Metasomatism of the shallow mantle beneath Yemen by the Afar plume—implications for mantle plumes, flood volcanism and intraplate volcanism. Geology 26:431–434

Bedini RM, Bodinier J-L, Dautria J-M, Morten L (1997) Evolution of LILE-enriched small melt fractions in the lithospheric mantle: a case study from East African Rift. Earth Planet Sci Lett 153:67–83

Blundy J, Dalton J (2000) Experimental comparison of trace element partitioning between clinopyroxene and melt in carbonate and silicate systems, and implications for mantle metasomatism. Contrib Mineral Petrol 139:356–371

Blundy JD, Wood BJ (1994) Prediction of crystal-melt partition coefficients from elastic moduli. Nature 372:452–454

Blundy JD, Robinson JAC, Wood BJ (1998) Heavy REE are compatible in clinopyroxene on the spinel-lherzolite solidus. Earth Planet Sci Lett 160:493–504

Bodinier J-L, Merlet C, Bedini RM, Simien F, Remaïdi M, Garrido CJ (1996) Distribution of niobium, tantalum and other highly incompatible trace elements in the lithospheric mantle: the spinel paradox. Geochim Cosmochim Acta 60:545–550

Bodinier J-L, Menzies MA, Shimizu N, Frey A, McPherson E (2004) Silicate, hydrous and carbonate metasomatism at Lherz, France: contemporaneous derivatives of silicate melt-harzburgite reaction. J Petrol 45:299–320

Brey GP, Köhler TP (1990) Geothermobarometry in four-phase lherzolites. II. New thermobarometers, and practical assessment of existing thermobarometers. J Petrol 31:1353–1378

Chalot-Prat F, Arnold M (1999) Immiscibility between calciocarbonatitic and silicate melts and related wall rock reactions in the upper mantle: a natural case study from Romanian mantle xenoliths. Lithos 46:627–659

Chazot G, Menzies M, Harte B, Mattey D (1994) Carbonatite metasomatism and melting of the Arabian lithosphere: evidence from oxygen isotopes and trace element composition of spinel lherzolites. Mineral Mag 58A:207–208

Chazot G, Menzies M, Harte B (1996) Determination of partition coefficients between apatite, clinopyroxene, amphibole, and melt in natural spinel lherzolites from Yemen: implications for wet melting of the lithospheric mantle. Geochim Cosmochim Acta 60:423–437

Dalton JA, Wood BJ (1993) The composition of primary carbonate melts and their evolution through wallrock reaction in the mantle. Earth Planet Sci Lett 119:511–525

Dautria JM, Dupuy C, Takherist D, Dostal J (1992) Carbonate metasomatism in the lithospheric mantle: peridotitic xenoliths from a melilitic district of the Sahara basin. Contrib Mineral Petrol 111:37–52

Foley SF, Barth MG, Jenner GA (2000) Rutile/melt partition coefficients for trace elements and an assessment of the influence of rutile on the trace element characteristics of subduction zone magmas. Geochim Cosmochim Acta 64:933–938

Foley SF, Petibon CM, Jenner GA, Kjarsgaard BA (2001) High U/Th partitioning by clinopyroxene from alkali silicate and carbonatite metasomatism: an origin for Th/U disequilibrium in mantle melts? Terra Nova 13:104–109

Franzini M, Leoni L, Saitta M (1975) Revisione di una metodologia analitica per fluorescenza-X, basata sulla correzione completa degli effetti di matrice. Rend Soc It Mineral Petrol 31:365–379

Gaetani GA, Grove TL (1998) The influence of water on melting of mantle peridotite. Contrib Mineral Petrol 131:323–346

Gorring ML, Kay SM (2000) Carbonatite metasomatized peridotite xenoliths from southern Patagonia: implications for lithospheric processes and Neogene plateau magmatism. Contrib Mineral Petrol 140:55–72

Gorring ML, Kay SM (2001) Mantle processes and sources of Neogene slab window magmas from Southern Patagonia, Argentina. J Petrol 42:1607–1094

Green TH (1995) Significance of Nb/Ta as an indicator of geochemical processes in the crust-mantle system. Chem Geol 120:347–359

Green TH, Pearson NJ (1987) An experimental study of Nb and Ta partitioning between Ti-rich minerals and silicate liquids at high pressure and temperature. Geochim Cosmochim Acta 51:55–62

Green DH, Wallace ME (1988) Mantle metasomatism by ephemeral carbonatite melts. Nature 336:459–462

Green TH, Adam J, Sie SH (1992) Trace element partitioning between silicate minerals and carbonatite at 25 Kbar and application to mantle metasomatism. Mineral Petrol 46:179–184

Grégoire M, Moine BN, O'Reilly SY, Cottin JY, Giret A (2000a) Trace element residence and partitioning in mantle xenoliths metasomatized by highly alkaline, silicate- and carbonate-rich melts (Kerguelen Islands, Indian Ocean). J Petrol 41:477–509

Grégoire M, Lorand JP, O'Reilly SY, Cottin JY (2000b) Armalcolite-bearing, Ti-rich metasomatic assemblages in harzburgitic xenoliths from the Kerguelen Archipelago: implications for the oceanic mantle budget of high-field strength elements. Geochim Cosmochim Acta 64:673–694

Grégoire M, McInnes BIA, O'Reilly SY (2001) Hydrous metasomatism of oceanic sub-arc mantle, Lihir, Papua, New Guinea. Part 2. Trace element characteristics of slab-derived fluids. Lithos 59:91–108

Hart SR, Dunn T (1993) Experimental cpx/melt partitioning of 24 trace elements. Contrib Mineral Petrol 113:1–8

Hauri EH, Wagner TP, Grove TL (1994) Experimental and natural partitioning of Th, U, Pb and other trace elements between garnet, clinopyroxene and basaltic melts. Chem Geol 117:149–166

Hill E, Wood BJ, Blundy JD (2000) The effect of Ca-Tschermak component on trace element partitioning between clinopyroxene and silicate melt. Lithos 52:203–215

Hirose K, Kawamoto T (1995) Hydrous partial melting of lherzolite at 1 GPa: the effect of H_2O on the genesis of basaltic magmas. Earth Planet Sci Lett 133:463–473

Hofmann AW (1988) Chemical differentiation of the Earth: the relationship between mantle, continental crust, and oceanic crust. Earth Planet Sci Lett 90:297–314

Ionov DA (2004) Chemical variations in peridotite xenoliths from Vitim, Siberia: inferences for REE and Hf behaviour in the garnet-facies upper mantle. J Petrol 45:343–367

Ionov DA, Bodinier JL, Mukasa SB, Zanetti A (2002) Mechanisms and sources of mantle metasomatism: major and trace element compositions of peridotite xenoliths from Spitsbergen in the context of numerical modelling. J Petrol 43:1–41

Jenner GA, Longerich HP, Jackson SE, Fryer BJ (1990) ICP-MS—a powerful tool for high-precision trace-element analysis in Earth sciences: evidence from analysis of selected U.S.G.S. reference samples. Chem Geol 83:133–148

Jenner JA, Foley SF, Jackson SE, Green TH, Fryer BJ, Longerich HP (1993) Determination of partition coefficients for trace elements in high pressure-temperature experimental run products by laser ablation microprobe-inductively coupled plasma-mass spectrometry (LAM-ICP-MS). Geochim Cosmochim Acta 57:5099–5103

Johnson KTM, Dick HJB, Shimizu N (1990) Melting in oceanic upper mantle: an ion microprobe study of diopsides in Abyssal Peridotites. J Geophys Res 95:2661–2678
Kalfoun F, Ionov D, Merlet C (2002) HFSE residence and Nb/Ta ratios in metasomatised, rutile-bearing mantle peridotites. Earth Planet Sci Lett 199:49–65
Kelemen PB, Dick HB, Quick JE (1992) Formation of harzburgite by pervasive melt/rock reaction in the upper mantle. Nature 358:635–641
Kelemen PB, Shimizu N, Salters VJM (1995) Extraction of mid-ocean-ridge basalt from mantle by focused flow of melt in dunite channels. Nature 375:747–753
Kelemen PB, Hart SR, Bernstein S (1998) Silica enrichment in the continental upper mantle via melt/rock reaction. Earth Planet Sci Lett 164:387–406
Keppler H (1996) Constraints from partitioning experiments on the composition of subduction-zone fluids. Nature 380:237–240
Kinzler RJ (1997) Melting of mantle peridotite at pressures approaching the spinel to garnet transition: application to mid-ocean ridge basalt petrogenesis. J Geophys Res 102:853–874
Koga KT, Kelemen PB, Shimizu N (2001) Petrogenesis of the crust-mantle transition zone and the origin of lower crustal wehrlite in the Oman ophiolite. Geochem Geophys Geosyst 2: paper number 2000GC000132
Köhler TP, Brey GP (1990) Calcium exchange between olivine and clinopyroxene calibrated as a geothermobarometer for natural peridotites from 2 to 60 Kbar with applications. Geochim Cosmochim Acta 54:2375–2388
Kretz R (1983) Symbols for rock-forming minerals. Am Mineral 68:277–279
Laurora A, Mazzucchelli M, Rivalenti G, Vannucci R, Zanetti A, Barbieri MA, Cingolani CA (2001) Metasomatism and melting in carbonated peridotite xenoliths from the mantle wedge: the Gobernador Gregores case (Southern Patagonia). J Petrol 42:69–87
Leibniz GW (1704) Nouveaux essais sur l'entendement humain, IV, 16, Galtier Paris
Leoni L, Saitta M (1976) X-ray fluorescence analysis of 29 trace elements in rock and mineral standards. Rend Soc It Mineral Petrol 32:497–510
McDade P, Blundy JD, Wood BJ (2003) Trace element partitioning on the Tinaquillo lherzolite solidus at 1.5 GPa. Phys Earth Planet Interiors 139:129–147
Menzies MA, Rogers N, Tindle A, Hawkesworth CJ (1987) Metasomatic and enrichment processes in lithospheric peridotites, an effect of asthenosphere—lithosphere interaction. In: Menzies MA, Hawkesworth CJ (eds) Mantle metasomatism. Academic, London, Geology Series, pp 313–364
Moine BN, Grégoire M, O'Reilly SY, Sheppard SMF, Cottin JY (2001) High field strength element fractionation in the Upper Mantle: evidence from amphibole-rich composite mantle xenoliths from the Kerguelen Islands (Indian Ocean). J Petrol 42:2145–2167
Neumann E-R, Wulff-Pedersen E (1997) The origin of highly silicic glass in mantle xenoliths from the Canary Islands. J Petrol 38:1513–1539
Oberti R, Vannucci R, Zanetti A, Tiepolo M, Brumm RC (2000) A crystal chemical re-evaluation of amphibole/melt and amphibole/clinopyroxene D_{Ti} values in petrogenetic studies. Am Miner 85:417–419
Peslier AH, Francis D, Ludden J (2002) The lithospheric mantle beneath continental margins: melting and melt-rock reaction in Canadian Cordillera xenoliths. J Petrol 43:2013–2047
Qi Q, Taylor LA, Zhou XM (1995) Petrology and geochemistry of mantle peridotite xenoliths from SE China. J Petrol 36:55–79
Raffone N, Zanetti A, Chazot G, Pin C, Vannucci R (2004) Genesis of Mg- and Fe-rich wehrlites in the lithospheric mantle beneath Ibalrhatene (Azrou, Mid Atlas, Morocco). J Petrol (submitted)
Rapp RP, Shimizu N, Norman MD, Applegate GS (1999) Reaction between slab-derived melts and peridotite in the mantle wedge: experimental constraints at 3.8 GPa. Chem Geol 160:335–356
Rivalenti G, Mazzucchelli M, Girardi VAV, Vannucci R, Barbieri MA, Zanetti A, Goldstein SL (2000) Composition and processes of the mantle lithosphere in northeastern Brazil and Fernando de Noronha: evidence from mantle xenoliths. Contrib Mineral Petrol 138:308–325
Rivalenti G, Mazzucchelli M, Laurora A, Cuffì SIA, Zanetti A, Vannucci R, Cingolani CA (2004) The backarc mantle lithosphere in Patagonia, South America. J South Am Earth Sci 17(1) (submitted)
Rudnick RL, McDonough WF, Chappell BC (1993) Carbonatite metasomatism in the northern Tanzanian mantle. Earth Planet Sci Lett 114:463–475
Salters VJM, Longhi JE, Bizimis M (2002) Near mantle solidus trace element partitioning at pressures up to 3.4 GPa. G^3 3:1–23
Shaw DM (1970) Trace element fractionation during anatexis. Geochim Cosmochim Acta 34:237–243
Shaw CSJ (1999) Dissolution of orthopyroxene in basanitic magma between 0.4 and 2 Gpa: further implications for the origin of Si-rich alkaline glass inclusions in mantle xenoliths. Contrib Mineral Petrol 135:114–132
Stalder R, Foley SF, Brey GP, Horn I (1998) Minel-acqueous fluid partitioning of trace elements at 900–1,200°C and 3.0 GPa: new experimental data for garnet, cpx and rutile and implications for mantle metasomatism. Geochim Cosmochim Acta 62:1781–1801
Stimac J, Hickmott D (1994) Trace element partition coefficients for ilmenite, orthopyroxene and pyrrhotite in rhyolite determined by micro-PIXE analysis. Chem Geol 117:313–330
Stosch H-G, Seck HA (1980) Geochemistry and mineralogy of two spinel peridotite suites from Dreiser Weiher, West Germany. Geochim Cosmochim Acta 44:457–470
Sun S-S, McDonough WF (1989) Chemical and isotopic systematics of ocean basalts: implications for mantle composition and processes. In: Saunders AD, Norry MJ (eds) Magmatism in the Ocean Basins. Geol Soc Spec Publ 42:313–345
Sweeney RJ, Green DH, Sie SH (1992) Trace and minor element partitioning between garnet and amphibole and carbonatitic melt. Earth Planet Sci Lett 113:1–14
Sweeney RJ, Prozesky V, Przybylowicz W (1995) Selected trace and minor element partitioning between peridotite minerals and carbonatite melts at 18–46 Kbar pressure. Geochim Cosmochim Acta 59:3671–3683
Tiepolo M, Vannucci R, Oberti R, Foley S, Bottazzi P, Zanetti A (2000) Nb and Ta incorporation and fractionation in Ti-rich pargasite and kaersutite: crystal-chemical constraints and implications for natural systems. Earth Planet Sci Lett 176: 185–201
Tiepolo M, Bottazzi P, Foley S, Oberti R, Vannucci R, Zanetti A (2001) Fractionation of Nb and Ta from Zr and Hf at Mantle Depths: the role of titanian pargasite and kaersutite. J Petrol 42:221–232
Tiepolo M, Oberti R, Vannucci R (2002) Trace-element incorporation in titanite: constraints from experimentally determined solid/liquid partition coefficients. Chem Geol 191:105–119
Vannucci R, Piccardo GB, Rivalenti G, Zanetti A, Rampone E, Ottolini L, Oberti R, Mazzucchelli M, Bottazzi P (1995) Origin of LREE-depleted amphiboles in the subcontinental mantle. Geochim Cosmochim Acta 59:1763–1771
Vannucci R, Bottazzi P, Wulff-Pedersen E, Neumann E-R (1998) Partitioning of REE, Y, Sr, Zr and Ti between clinopyroxene and silicate melts in the mantle under La Palma (Canary Islands): implications for the nature of the metasomatic agents. Earth Planet Sci Lett 158:39–51
Vernières J, Godard M, Bodinier J-L (1997) A plate model for the simulation of trace element fractionation during partial melting and magma transport in the Earth's upper mantle. J Geophys Res 102:24771–24784
Wallace ME, Green DH (1988) An experimental determination of primary carbonatite composition. Nature 335:345–346
Walter MJ (1998) Melting of garnet peridotite and the origin of komatiite and depleted lithosphere. J Petrol 39:28–60
Wendlandt RF, Harrison WJ (1979) Rare earth partitioning between immiscible carbonate and silicate liquids and CO2

vapour: results and implications for the formation of Light Rare Earth-enriched rocks. Contrib Mineral Petrol 69:409–419
van Westrenen W, Blundy JD, Wood BJ (2001) High field strength element/rare earth element fractionation during partial melting in the presence of garnet: implications for identification of mantle heterogeneities. Geochem Geophys Geosyst G^3: 2
Wulff-Pedersen E, Neumann, E-R, Vannucci R, Bottazzi P, Ottolini L (1999) Silicic melts produced by reaction between peridotite and infiltrating basaltic melts: ion probe data on glasses and minerals in veined xenoliths from La Palma, Canary Islands. Contrib Mineral Petrol 137:59–82
Xu YG, Mercier J-CC, Menzies MA, Ross JV, Harte B, Lin C, Shi L (1996) K-rich glass-bearing wehrlite xenoliths from Ytong, Northeastern China: petrological and chemical evidence for mantle metasomatism. Contrib Mineral Petrol 125:406–420
Xu X, O'Reilly SY, Griffin WL, Zhou X (2000) Genesis of young lithospheric mantle in southeastern China. J Petrol 41:111–148
Yaxley GM, Green DH (1996) Experimental reconstruction of sodic dolomitic carbonatite melts from metasomatised lithosphere. Contrib Mineral Petrol 124:359–369
Yaxley GM, Green DH (1998) Reactions between eclogite and peridotite: mantle refertilisation by subduction of oceanic crust. Schweiz Mineral Petrogr Mitt 78:243–255
Yaxley GM, Kamenetsky V (1999) In situ origin for glass in mantle xenoliths from southeastern Australia: insights from trace element compositions of glasses and metasomatic phases. Earth Planet Sci Lett 172:97–109
Yaxley GM, Crawford AJ, Green DH (1991) Evidence for carbonatite metasomatism in spinel peridotite xenoliths from western Victoria, Australia. Earth Planet Sci Lett 107:305–317
Zanetti A, Mazzucchelli M, Rivalenti G, Vannucci R (1999) The Finero phlogopite-peridotite massif: an example of subduction-related metasomatism. Contrib Mineral Petrol 134:107–122
Zinngrebe E, Foley SF (1995) Metasomatism in mantle xenoliths from Gees, West Eifel, Germany: evidence for the genesis of calc-alkaline glasses and metasomatic Ca-enrichment. Contrib Mineral Petrol 122:79–96